

Evidence for Residual Melt Extraction in the Takidani Pluton, Central Japan

Eva Hartung^{1*}, Luca Caricchi¹, David Floess¹, Simon Wallis², Satoru Harayama³, Kalin Kouzmanov¹ and Massimo Chiaradia¹

¹Department of Earth Sciences, University of Geneva, 1205 Geneva, Switzerland; ²Department of Earth and Planetary Sciences, Nagoya University, Nagoya 464-8601, Japan; and ³Department of Geology, Shinshu University, Matsumoto 390-8621, Japan

*Corresponding author. Telephone: +41 (0)22 379 66 97. Fax: +41 (0)22 379 03 29. E-mail: eva.hartung@unige.ch

Received October 5, 2016; Accepted May 19, 2017

ABSTRACT

The Takidani pluton represents one of a few locations where melt extraction from a crystal mush is preserved in the natural rock record, making it an extremely good case study for investigating the generation of evolved melt reservoirs in the upper crust. Located in the Japan Alps, the Takidani pluton shows a clear vertical zonation consisting of granite and granodiorite in the lower and middle section, a fine-grained porphyritic granitic unit in the upper section and a marginal granodiorite at the roof contact with the host-rock. We present a detailed petrographic and geochemical study using samples collected along a section that traverses the entire vertical section of the pluton. No sharp contacts are found between units. Instead, gradual changes in rock fabric and mineralogy are observed between the lower granodiorite and overlying porphyritic unit. Major and trace element bulk-rock compositions show sigmoidal variations from the bottom to top of the pluton. Incompatible elements and silica contents increase roofwards within the porphyritic unit. Plagioclase chemistry reveals three main crystal populations (P1, P2 and P3) with Fe contents increasing towards the base of the pluton. Comparison with existing crystallization experiments, thermobarometry and hygrometry indicate that the magmas were emplaced at around 200 MPa, 850–900°C and bulk water contents of 3–4 wt %. Whole-rock major and trace element analyses together with mineral chemistry and textural observations suggest that the fine-grained porphyritic unit was extracted from the underlying granodiorite at temperatures between 800 and 740°C and crystallinities of 45–65 wt %. Radiogenic isotopes indicate only minor assimilation (2–6 wt %) and support melt evolution through crystal fractionation. The fine-grained matrix of the porphyritic unit may have been the result of pressure quenching associated with a volcanic eruption.

Key words: melt segregation; melt evolution; crystal mush; granodiorite; granite

INTRODUCTION

The segregation of residual melt from partially crystallized and rheologically locked magmas (Marsh, 1981; Brophy, 1991; Vigneresse *et al.*, 1996) is a process that can lead to the formation of crystal-poor and potentially eruptible pockets of magma in the upper crust (Bachmann & Bergantz, 2004, 2008; Hildreth, 2004; Dufek & Bachmann, 2010; Deering *et al.*, 2011). A variety of petrographic and geochemical observations (Hildreth & Wilson, 2007; Barboni & Schoene, 2014; Cashman & Giordano, 2014; Ellis *et al.*, 2014; Wotzlaw *et al.*, 2014; Christopher *et al.*,

2015) and numerical analysis (Bachmann & Bergantz, 2004; Dufek & Bachmann, 2010; Solano *et al.*, 2012) have illustrated that melt extraction is a common process in volcanic sequences. Nevertheless, evidence for large-scale melt extraction and accumulation is rarely found in intrusive magma bodies (Coleman *et al.*, 2012). This may reflect the ephemeral nature of such melt-rich magma lenses, as suggested by thermal modelling (Annen, 2009; Annen *et al.*, 2015).

Segregated melt may be difficult to recognize in the field if it crystallizes at similar rates to the surrounding

magma and generates holocrystalline rock textures. The thermal structure and evolution of melt reservoirs, together with phase petrology and especially the relationships between temperature and crystallinity, control the timespan a magma spends at conditions favourable for melt segregation (Marsh, 1981; Dufek & Bachmann, 2010; Melekhova *et al.*, 2013; Caricchi & Blundy, 2015). The low duration of this period results in a relatively low probability of finding evidence for melt segregation in the intrusive record. A final but nonetheless important point is that plutons are the accumulated product of numerous incremental injections of magma (Glazner *et al.*, 2004; de Saint-Blanquat *et al.*, 2006; Menand *et al.*, 2015) and this periodic replenishing of hot magma tends to obliterate earlier fabrics and chemical heterogeneities (Paterson *et al.*, 1998; Zak *et al.*, 2007).

The Takidani pluton (TK) is an extremely good candidate to study the extraction of residual melt from magmatic mushes because of its chemical stratification and the gradual transition from holocrystalline textures at the intrusion's base and centre to porphyritic textures towards the roof contact (Harayama, 1992; Bando *et al.*, 2003). Here we present the results of whole-rock major and trace element and isotopic analyses for samples collected along a complete section along the Shiradashi-zawa valley, in combination with the mineral chemistry of various minerals at different levels within the intrusion. The main goal of this study is to investigate the dominant processes responsible for the chemical zoning and evolution in the upper part of the TK.

THE TAKIDANI PLUTON

Geology

The TK is located in the Hida Mountain Range along the main axis of the Japan Alps where it crops out in a north-south elongated lozenge shape (Fig. 1a; Harayama, 1990, 1992, 1994; Bando & Tsuchiya, 2000; Bando *et al.*, 2003).

The pluton is located in the active Norikura Volcanic Chain between Yake Lake and Hotaka Lake (Fig. 1a) and covers an area of $\sim 21 \text{ km}^2$ (Harayama, 1992). Along its western margin, the TK is tectonically juxtaposed with Mesozoic basement and Paleogene granitic rocks. On its eastern margin it borders the Late Pliocene Hotaka Andesite (2.4 Ma; Yamada *et al.*, 1985; Harayama, 1990) with a magmatic contact formed during the intrusion of the felsic melts forming the TK. To the south the TK is unconformably overlain by the Quaternary volcanic deposits of Mount Yake. The TK was rapidly uplifted ($5.1\text{--}5.9 \text{ mm a}^{-1}$; Bando *et al.*, 2003) and tilted eastwards resulting in a nearly vertical contact on its western side and a shallow eastwards dipping contact of about 20° on its eastern side (Harayama, 1994). The vertical thickness of the outcropping portion of the TG is estimated to be between 1200 and 1800 m (Bando *et al.*, 2003; Harayama *et al.*, 2003).

The pluton is vertically zoned varying from fine-grained biotite (bt)-granite (fGT) and medium-grained hornblende (hbl)-bt-granite (GRT) in the lower section of the pluton, to medium-grained hbl-bt-granodiorite (GDT) in the middle section (Fig. 1b; Harayama, 1992; Harayama *et al.*, 2003). In the upper section, GDT marks the transition into fine-grained porphyritic granodiorite and granite (pGT). The marginal unit at the roof of the pluton is a coarse-grained porphyritic granodiorite (mGT; Bando & Tsuchiya, 2000; Bando *et al.*, 2003; Harayama *et al.*, 2003). Rocks of the fGT are dominantly found along the basal contact (Bando & Tsuchiya, 2000; Bando *et al.*, 2003), but a similar lithology has been identified near the roof contact in the southern part of the pluton (Harayama *et al.*, 2003).

Geochronology

U-Pb zircon isochron ages range between 1.36 and 1.54 Ma ($\pm 0.23 \text{ Ma}$; Sano *et al.*, 2002) whereas zircon fission-track ages (effective closure temperature $240^\circ\text{C} \pm 30^\circ\text{C}$; Bernert & Garver, 2005) yield an age of 0.80 Ma ($\pm 0.02 \text{ Ma}$; Harayama,

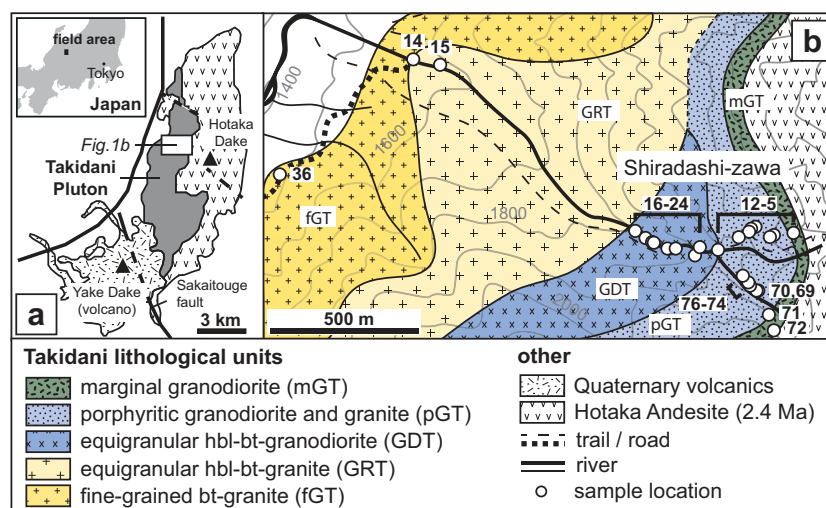


Fig. 1. (a) Location of the Takidani Pluton (TK) in central Honshu, modified after Harayama *et al.* (2003). (b) Geological map of the Shiradashi-zawa valley including sample locations and topographic contour lines.

1990, 1992, 1994). K–Ar ages of hornblende, biotite and alkali feldspar vary from 1.43 Ma (± 0.12 Ma) to 1.94 Ma (± 0.21 Ma), from 1.07 Ma (± 0.04 Ma) to 1.27 Ma (± 0.06 Ma) and from 1.07 Ma (± 0.06 Ma) to 1.23 Ma (± 0.06 Ma), respectively (Harayama, 1992, 1994). Most K–Ar mineral ages are consistent with the zircon crystallization ages. The significance of the older hornblende K–Ar ages is less clear but they may reflect the presence of extraneous ^{40}Ar (Harayama *et al.*, 2003).

Studies constraining the temperature–time path of the TK have suggested a two-stage cooling history with an initial rapid rate of about $150^\circ\text{C ka}^{-1}$ followed by slower cooling rates of about 40°C ka^{-1} (Harayama, 1992, 1994; Kano *et al.*, 2000; Tsuchiya & Fujino, 2000; Sano *et al.*, 2002). The presence of a magmatic contact with the Hotaka Andesite and the results of thermochronological studies show that the TK magmatic reservoir was emplaced after the Hotaka Andesite (Harayama, 1992, 1994), but before eruption of the 1.76 Ma (± 0.17 Ma) Nyukawa Pyroclastic Flow Deposit (PFD; Harayama *et al.*, 1991) and the 10 kyr younger Chayano–Ebisutoge Pyroclastic Deposits (PD; Nagahashi, 1995; Nagahashi *et al.*, 1996, 2000; Kataoka *et al.*, 2001; Kimura & Nagahashi, 2007).

Previous work has predominantly focused on the emplacement and cooling history of the TK. In this study, we focus on the magmatic processes that can be identified based on petrographic, geochemical and structural investigation of the TK. This pluton offers an extremely rare opportunity to examine the petrogenetic processes within a young and well-exposed zoned crustal magmatic body.

SAMPLING STRATEGY AND FIELD OBSERVATIONS

The TK lies within a rugged mountain terrain in the Chubu Sangaku National Park. It is exposed at elevations between about 1400 and 2500 m, especially along steep valleys (i.e. Shiradashi-zawa, Yanagani-dani, Takidani). In many places, large parts of the outcrops are covered under scree fields. Mountain slopes are generally about 40° and change into nearly vertical rock faces at higher elevations.

During our field campaign in 2014 we collected a total of 101 samples along four NW–SE-trending river valleys in the northern section of the TK and along mountain ridges in the southern part of the intrusion, to characterize the lithofacies and variability observed in rock textures and mineralogy from the base (west) to the roof (east) of the intrusion. The exposure along the Shiradashi-zawa valley provides a complete cross-section of the entire pluton where a gradual transition from the equigranular to fine-grained porphyritic units (i.e. GDT to pGT) is observed towards the roof (Fig. 1b). In this study we present petrographic and geochemical data for 25 rock samples collected along or close to (e.g. location 36; Fig. 1b) the Shiradashi-zawa valley. This cross-section represents not only the most representative transect across the TK but is also critical to

understanding the processes responsible for the transitions in rock fabric and mineralogy seen from GDT to pGT in the upper part of the intrusion.

ANALYTICAL METHODS

Whole-rock analyses

Bulk-rock major and trace element analyses were performed for 25 samples collected along the Shiradashi-zawa valley (Fig. 1b; Table 1). Neodymium, Sr and Pb isotopes were analysed for 12 of these samples. Major elements were determined by X-ray fluorescence (XRF) using a PANalytical AXIOS MAX with a rhodium anode tube at 4 W at the University of Lausanne. SY-2, JCH-1, NIM-N and NIM-G standards were used for quality control. Trace element concentrations were measured using glass beads by laser ablation inductively coupled plasma mass spectrometry (LA-ICP-MS) using a Quadrupole Agilent 7700 spectrometer interfaced to a GeoLas 200 M 193 nm excimer ablation system at the University of Lausanne. The system was operating at 1420 W with a laser repetition rate of 10 Hz and a $120\text{ }\mu\text{m}$ spot size. Each sample was measured three times for 60 s. The background was measured for 90 s before the three ablations. Trace element concentrations were recalculated using CaO contents from XRF analyses as an internal standard with reference to the NIST SRM 612 external standard. Data reduction was performed using the LAMTrace software (Jackson *et al.*, 1992; Longerich *et al.*, 1996; Jackson, 2008a, 2008b).

Radiogenic isotopes of Sr, Nd and Pb were analysed at the University of Geneva using a Thermo Neptune PLUS Multi-Collector ICP-MS system following the methods described by Chiaradia *et al.* (2011). Isotopic ratios were corrected for internal fractionation using $^{88}\text{Sr}/^{86}\text{Sr} = 8.375209$ for the $^{87}\text{Sr}/^{86}\text{Sr}$ ratio, $^{146}\text{Nd}/^{144}\text{Nd} = 0.7219$ for the $^{143}\text{Nd}/^{144}\text{Nd}$ ratio and $^{203}\text{Tl}/^{205}\text{Tl} = 0.418922$ for the three Pb ratios (a Tl standard was added to the solution). SRM987 ($^{87}\text{Sr}/^{86}\text{Sr} = 0.710248$, long-term external reproducibility: 10 ppm), JNdi-1 ($^{143}\text{Nd}/^{144}\text{Nd} = 0.512115$; Tanaka *et al.*, 2000; long-term external reproducibility: 10 ppm), and SRM 981 (Pb-isotopes; Baker *et al.*, 2004; long-term external reproducibility of 0.0048% for $^{206}\text{Pb}/^{204}\text{Pb}$, 0.0049% for $^{207}\text{Pb}/^{204}\text{Pb}$ and 0.0062% for $^{208}\text{Pb}/^{204}\text{Pb}$) were used as external standards. Owing to a systematic difference between measured and accepted standard ratios Sr, Nd and Pb isotope ratios were further corrected for external fractionation by a value of -0.039 , $+0.047$ and $+0.5$ a.m.u., respectively. Mass interferences at 84 (^{84}Kr), 86 (^{86}Kr) and 87 (^{87}Rb) were corrected for by monitoring ^{83}Kr and ^{85}Rb . The interference of ^{144}Sm on ^{144}Nd was monitored on ^{147}Sm and corrected with a value of 0.206700 ($^{144}\text{Sm}/^{147}\text{Sm}$); the interference of ^{204}Hg on ^{204}Pb was corrected by monitoring ^{202}Hg .

Mineral chemistry

Mineral analyses were performed with a JEOL 8200 Superprobe electron microprobe analyser (EMPA) at

Table 1: Major and trace elements and radiogenic isotopes of samples from the Takidani pluton along Shiradashi-zawa

	Unit:	mGT EH5	pGT EH6	pGT EH7	pGT EH9	pGT EH10	pGT EH11	pGT EH12	GRT EH14	GRT EH15	GDT EH16	GDT EH17	GDT EH18	GDT EH19
ID:		36-2936	36-2936	36-2935	36-2939	36-2937	36-2925	36-2928	36-3001	36-2998	36-2937	36-2937	36-2934	36-2933
Latitude (°N):		137-6310	137-6301	137-6300	137-6292	137-6290	137-6281	137-6275	137-6139	137-6153	137-6238	137-6242	137-6247	137-6248
Elevation (m):		2186	2113	2092	2040	2024	2020	1949	1549	1573	1805	1816	1827	1828
wt %														
SiO ₂	67.83	69.21	69.55	69.71	69.02	69.99	66.76	67.24	66.54	67.24	64.74	64.32	65.41	65.12
TiO ₂	0.54	0.40	0.42	0.45	0.47	0.38	0.57	0.58	0.55	0.58	0.67	0.71	0.61	0.67
Al ₂ O ₃	14.97	14.12	14.38	14.35	14.84	14.13	15.13	14.82	15.27	14.82	15.41	15.42	15.31	15.29
Fe ₂ O ₃	3.85	3.88	3.40	3.13	3.18	3.13	4.26	4.11	3.86	4.11	4.97	5.24	4.51	4.91
MnO	0.08	0.09	0.08	0.04	0.05	0.06	0.09	0.08	0.09	0.08	0.09	0.10	0.09	
MgO	1.49	1.14	1.11	1.28	1.31	1.15	1.74	1.64	1.58	1.64	2.09	2.21	1.95	2.05
CaO	3.60	2.88	2.81	2.99	3.38	2.78	3.88	3.70	3.99	3.70	4.49	4.52	4.27	4.38
Na ₂ O	3.65	3.49	3.45	3.32	3.53	3.30	3.57	3.44	3.47	3.44	3.36	3.44	3.36	3.41
K ₂ O	2.93	3.74	3.81	3.41	3.31	3.64	3.11	3.31	3.25	3.31	2.89	2.80	3.10	2.85
P ₂ O ₅	0.16	0.11	0.11	0.12	0.12	0.11	0.16	0.15	0.15	0.15	0.18	0.20	0.17	0.18
LOI	0.31	0.23	0.31	0.45	0.49	0.56	0.29	0.26	0.63	0.26	0.34	0.61	0.46	0.46
Total	99.40	99.29	99.42	99.26	99.71	99.24	99.55	99.33	99.37	99.33	99.23	99.57	99.23	99.31
ppm														
Sc	11.1	10.8	9.4	10.6	9.8	10.4	13.0	12.7	11.5	12.7	14.1	15.0	12.9	14.1
Co	7.1	6.0	6.3	6.3	5.7	6.3	8.6	8.1	8.5	8.1	10.2	10.9	9.5	10.4
Ni	5.0	4.2	3.1	3.6	3.8	3.7	4.8	5.3	5.9	5.3	6.8	7.0	9.9	6.1
Cu	15.5	10.7	47.9	6.6	4.4	5.9	7.4	8.2	5.9	8.2	11.0	7.5	10.6	9.8
Zn	32.1	36.6	45.3	22.2	21.4	27.7	50.8	40.8	44.5	40.8	46.1	51.4	45.9	49.5
Rb	88	106	117	113	95	107	99	106	101	106	88	88	93	91
Sr	312	261	232	253	281	249	294	282	323	282	340	336	327	337
Y	19.9	13.4	15.7	14.6	14.6	14.9	19.4	21.6	17.4	21.6	17.9	19.4	17.8	18.5
Zr	150	120	118	124	118	126	139	169	151	169	154	156	149	147
Nb	7.9	7.5	7.8	7.7	7.1	7.8	8.8	8.5	7.2	8.5	7.6	7.8	7.2	7.8
Mo	0.2	2.2	0.9	0.3	0.3	5.1	0.6	0.4	0.5	0.4	0.6	1.0	0.4	0.9
Cs	2.6	2.0	3.2	4.3	2.7	2.5	4.9	3.9	1.7	3.9	4.8	4.3	3.1	3.3
Ba	506	527	465	448	498	451	418	507	570	507	485	482	471	481
La	23.5	22.9	29.1	28.6	27.8	25.8	31.6	30.8	26.9	30.8	23.1	28.7	29.5	24.6
Ce	44.9	41.7	52.5	51.6	50.5	46.5	59.9	60.4	51.4	60.4	46.5	56.0	56.6	48.3
Pr	5.2	4.2	5.2	5.0	5.1	4.7	6.1	6.5	5.4	6.5	5.1	6.1	6.0	5.2
Nd	19.5	15.2	18.3	17.4	17.9	16.4	22.5	23.8	19.5	23.8	19.5	22.8	22.4	20.3
Sm	3.8	2.7	3.1	3.1	3.0	2.9	4.0	4.5	3.5	4.5	3.8	4.3	3.9	3.7
Eu	1.0	0.7	0.8	0.8	0.8	0.7	0.9	0.9	0.9	0.9	1.0	1.1	1.0	1.0
Gd	3.4	2.5	2.7	2.6	2.7	2.7	3.6	3.6	3.1	3.9	3.4	3.8	3.4	3.5
Tb	0.5	0.4	0.4	0.4	0.4	0.4	0.5	0.5	0.5	0.6	0.5	0.5	0.5	0.5
Dy	3.3	2.3	2.7	2.5	2.5	2.4	3.3	3.8	3.0	3.8	3.2	3.6	3.2	3.2
Ho	0.7	0.5	0.5	0.5	0.5	0.5	0.7	0.8	0.6	0.8	0.6	0.7	0.6	0.7
Er	2.0	1.4	1.7	1.5	1.5	1.5	2.0	2.3	1.8	2.3	1.9	2.0	1.8	1.9
Tm	0.3	0.2	0.3	0.2	0.2	0.2	0.3	0.3	0.3	0.3	0.3	0.3	0.3	0.3
Yb	2.1	1.6	2.0	1.8	1.8	1.8	2.3	2.5	2.0	2.5	2.1	2.2	2.0	2.1
Lu	0.3	0.2	0.3	0.3	0.3	0.3	0.4	0.4	0.3	0.4	0.3	0.3	0.3	0.3
Hf	4.2	3.5	3.5	3.7	3.4	3.7	4.0	4.7	4.1	4.7	4.2	4.3	4.1	4.0
Ta	0.7	0.8	0.9	0.9	0.7	0.9	1.0	0.8	0.6	0.8	0.7	0.7	0.7	0.7
W	0.9	0.5	1.7	0.4	0.5	0.5	1.8	1.1	1.0	1.1	1.2	1.0	1.1	0.8
Pb	8.4	14.1	16.2	9.4	9.5	9.3	15.6	11.8	15.4	11.8	11.7	13.7	11.5	11.5
Th	11.7	15.8	19.6	17.5	14.7	19.2	16.8	16.3	12.5	16.3	10.7	10.4	12.1	11.8
U	2.7	3.3	4.3	3.7	3.3	3.8	3.9	3.2	2.6	3.2	2.3	2.2	2.5	2.5
¹⁴³ Nd/ ¹⁴⁴ Nd	0.512463	0.512543				0.512514	0.512500		0.512529	0.512584			0.512488	
⁸⁷ Sr/ ⁸⁶ Sr	0.707535	0.707243				0.707234	0.707228		0.707149	0.707085			0.707161	
²⁰⁶ Pb/ ²⁰⁴ Pb	18.39539	18.40343				18.40059	18.40217		18.39883	18.39716			18.40050	
²⁰⁷ Pb/ ²⁰⁴ Pb	15.61338	15.62013				15.61529	15.61648		15.61580	15.61366			15.61496	
²⁰⁸ Pb/ ²⁰⁴ Pb	38.77705	38.78723				38.77786	38.77863		38.77249	38.75889			38.77153	

Downloaded from <https://academic.oup.com/petrology/article/58/4/763/3979505> by guest on 21 August 2022

Table 1: Continued

Unit:	GDT	GDT	GDT	GDT	fGT	pGT	pGT	mGT	mGT	pGT	pGT	pGT
ID:	EH20	EH21	EH23	EH24	EH36	EH69	EH70	EH71	EH72	EH74	EH75	EH76
Latitude (°N):	36.2931	36.2931	36.2933	36.2931	36.2957	36.2916	36.2918	36.2907	36.2901	36.2918	36.2919	36.2921
Longitude (°E):	137.6253	137.6257	137.6262	137.6266	137.6078	137.6294	137.6293	137.6299	137.6301	137.6291	137.6290	137.6287
Elevation (m):	1849	1864	1879	1892	1478	2040	2035	2110	2160	2020	2010	1995
wf %												
SiO ₂	64.28	65.59	65.38	64.92	73.48	68.88	69.25	67.68	67.41	67.38	66.43	67.03
TiO ₂	0.71	0.63	0.67	0.68	0.28	0.48	0.41	0.55	0.59	0.54	0.56	0.54
Al ₂ O ₃	15.22	15.28	15.17	15.39	13.31	14.67	14.72	14.64	14.88	14.95	15.14	14.84
Fe ₂ O ₃	5.28	4.67	5.01	5.07	2.39	3.45	3.27	4.11	4.22	4.01	4.23	4.02
MnO	0.10	0.09	0.10	0.09	0.05	0.05	0.06	0.08	0.08	0.06	0.05	0.06
MgO	2.24	1.92	2.13	2.14	0.51	1.37	1.27	1.51	1.58	1.63	1.70	1.60
CaO	4.56	4.34	4.45	4.38	1.59	3.28	3.25	3.47	3.60	3.79	3.66	3.67
Na ₂ O	3.35	3.39	3.39	3.16	3.45	3.12	3.28	3.40	3.64	3.08	2.83	3.31
K ₂ O	2.94	2.96	2.81	2.87	4.32	3.28	3.50	3.26	3.04	3.29	2.99	3.29
P ₂ O ₅	0.20	0.18	0.19	0.19	0.08	0.13	0.12	0.16	0.17	0.15	0.16	0.15
LOI	0.59	0.31	0.44	0.66	0.52	0.46	0.35	0.37	0.27	0.41	1.39	0.50
Total	99.46	99.36	99.73	99.54	99.97	99.18	99.47	99.22	99.47	99.29	99.14	99.02
ppm												
Sc	15.2	13.4	14.7	14.1	8.9	10.1	9.9	11.2	11.3	11.6	11.8	11.8
Co	11.1	9.7	10.4	10.6	2.4	6.9	6.0	7.8	7.7	8.0	8.5	7.3
Ni	6.8	6.0	7.0	5.9	3.7	4.5	4.4	4.4	3.8	4.7	4.2	5.4
Cu	9.1	9.9	8.2	8.9	9.5	18.7	5.5	4.7	3.0	28.8	28.4	8.0
Zn	47.1	48.7	48.8	50.9	72.6	25.4	28.7	35.1	40.8	29.2	28.1	28.0
Rb	93	88	89	93	114	119	108	95	94	107	92	104
Sr	330	330	328	334	173	267	266	302	314	288	306	292
Y	20.0	18.3	19.5	19.4	19.2	16.7	16.2	18.1	18.9	18.0	17.0	17.9
Zr	155	157	153	158	168	130	131	149	153	137	135	139
Nb	8.2	7.7	8.0	7.7	8.1	8.3	7.9	8.0	8.7	8.1	7.5	8.1
Mo	0.6	0.6	0.7	0.6	0.5	11.7	1.9	0.5	0.4	6.1	0.5	0.5
Cs	3.5	2.8	3.2	3.9	2.3	5.9	5.4	2.6	3.3	4.8	4.5	4.0
Ba	512	480	448	490	674	470	471	546	533	445	480	491
La	37.6	25.0	23.4	25.1	35.7	31.2	28.6	37.5	28.5	29.3	23.5	27.2
Ce	70.1	49.1	46.4	49.2	71.6	56.5	52.6	69.3	55.6	54.7	44.5	51.2
Pr	7.1	5.3	5.2	5.4	7.5	5.7	5.3	7.0	5.9	5.6	4.7	5.3
Nd	26.0	20.2	20.1	20.8	26.8	19.7	18.0	25.1	21.6	20.1	18.0	19.3
Sm	4.5	3.8	3.9	4.0	4.1	3.4	3.2	4.1	3.9	3.7	3.4	3.6
Eu	1.1	1.0	1.0	1.0	0.7	0.8	0.8	1.0	0.9	0.9	0.9	0.9
Gd	4.0	3.4	3.5	3.5	3.6	2.8	2.8	3.4	3.5	3.2	3.1	3.2
Tb	0.6	0.5	0.5	0.5	0.5	0.4	0.4	0.5	0.5	0.5	0.4	0.5
Dy	3.7	3.3	3.5	3.5	3.4	2.9	2.8	3.3	4.4	3.1	3.0	3.1
Ho	0.7	0.6	0.7	0.7	0.7	0.6	0.5	0.6	0.7	0.6	0.6	0.6
Er	2.1	1.9	2.1	2.0	2.0	1.8	1.6	1.9	2.0	1.9	1.8	1.8
Tm	0.3	0.3	0.3	0.3	0.3	0.3	0.3	0.3	0.3	0.3	0.3	0.3
Yb	2.2	2.1	2.2	2.2	2.2	2.0	1.9	2.0	2.1	2.2	2.0	2.0
Lu	0.3	0.3	0.3	0.3	0.4	0.3	0.3	0.3	0.3	0.3	0.3	0.3
Hf	4.1	4.4	4.2	4.3	5.1	3.9	3.8	4.0	4.1	4.1	3.9	3.9
Ta	0.7	0.7	0.7	0.7	0.9	0.7	0.9	0.7	0.7	0.8	0.7	0.8
W	0.8	0.8	1.2	1.1	0.5	0.7	0.9	0.4	0.4	0.4	0.7	0.6
Pb	11.1	13.8	10.8	10.7	14.9	9.3	12.5	9.3	9.3	11.1	12.4	10.5
Th	10.5	13.0	11.1	11.2	13.6	17.8	17.4	14.0	11.5	15.7	13.9	15.1
U	2.2	2.8	2.5	2.4	3.0	3.8	3.9	2.4	2.4	3.5	3.1	3.3
¹⁴³ Nd/ ¹⁴⁴ Nd	0.51249	0.51252	0.51249	0.51249	0.51249	0.51249	0.51249	0.51249	0.51253	0.51249	0.51249	0.51254
⁸⁷ Sr/ ⁸⁶ Sr	0.70718	0.70715	0.70715	0.70715	0.70715	0.70715	0.70715	0.70715	0.70715	0.70715	0.70715	0.70732
²⁰⁶ Pb/ ²⁰⁴ Pb	18.3965	18.3988	18.3988	18.3988	18.3988	18.3988	18.3988	18.3988	18.4079	18.4079	18.4079	18.4026
²⁰⁷ Pb/ ²⁰⁴ Pb	15.6159	15.6140	15.6140	15.6140	15.6159	15.6159	15.6159	15.6159	15.6251	15.6251	15.6251	15.6169
²⁰⁸ Pb/ ²⁰⁴ Pb	38.7686	38.7685	38.7685	38.7685	38.7686	38.7686	38.7686	38.7686	38.8061	38.8061	38.8061	38.7783

LOI, loss on ignition.

the University of Lausanne. The microprobe is equipped with a five-channel wavelength-dispersive spectroscope system (WDS) and was operated at an accelerating voltage of 15 kV and a beam current of 15 nA. A defocused beam of 2 µm diameter was used for feldspar, amphibole and biotite analyses. Oxides were analysed with a beam diameter of 1 µm. Analyses with a maximum 1σ error of 1% were retained and additionally checked by calculating the appropriate mineral formula. Representative mineral analyses of plagioclase and amphibole are listed in Tables 2 and 3. Alkali feldspar, biotite and oxide data are provided in Supplementary Data Appendices A–D. All data and operating conditions are reported in Supplementary Data Appendix E. (Supplementary data are available for downloading at <http://www.petrology.oxfordjournals.org>.)

Quantitative evaluation of minerals by scanning electron microscopy (QEMSCAN)

Six thin sections were analysed by automated mineral analysis and textural imaging using an FEI QEMSCAN® Quanta 650 F at the University of Geneva. The system is equipped with two Bruker QUANTAX light-element energy-dispersive X-ray spectrometers. Analyses were conducted at high vacuum, accelerating voltage of 25 kV, and a probe current of 10 nA on carbon-coated polished thin sections. FieldImage operating mode (Pirrie *et al.*, 2004) was used for analyses. Two-hundred and twenty-one fields were measured per sample, with 1500 µm per field, and a point spacing of 5 µm. Data processing was performed using the iDiscover® software package to produce high-quality spatially resolved and fully quantified mineralogical maps. The modal abundances of mineral phases above 0.1 area % are listed in Table 4.

Plagioclase analyses from EMP sessions were used to assign anorthite contents to Ca intensities obtained from the EDX spectra during QEMSCAN analyses. To obtain anorthite distribution maps of plagioclase, other Ca-bearing phases, such as amphibole and apatite, were filtered out from the obtained Ca maps. Amphibole grains were grouped and subtracted from

the Ca distribution maps based on Fe intensities. Apatite grains were grouped and removed based on their high Ca intensity. Four plagioclase groups of different composition were then created using bins of 20 mol % anorthite (i.e. An_{10–30}, An_{30–50}, An_{50–70}, An_{70–90}). The area percentages of plagioclase bins are listed in Table 5. It should be noted that small differences (up to 8%) exist in three samples between the total area percentage of plagioclase from the QEMSCAN maps and plagioclase obtained from Ca-distribution maps.

PETROGRAPHY

Fine-grained bt-granite (fGT)

This unit crops out at the basal contact of the pluton and is markedly fine-grained (<1 mm; Fig. 2). Plagioclase is normally zoned and occasionally contains resorbed cores. Quartz shows undulose extinction and a mosaic texture. Alkali feldspar is interstitial and perthitic. Amphibole is entirely altered to biotite and iron oxides. Zircon is usually found within plagioclase and quartz; apatite is commonly included in quartz. Overall, the alteration of fGT is more profound with higher degrees of chloritization and oxidation.

Equigranular hbl–bt-granite (GRT)

GRT has a characteristic medium-grained equigranular texture (<5 mm; Fig. 2). Plagioclase crystals (<5 mm) are oscillatory zoned and surrounded by darker rims. Some crystals contain resorbed or patchy zoned cores. Amphibole (<2 mm) forms euhedral to subhedral grains that locally include euhedral plagioclase or magnetite. In the lower section of GRT, amphibole is almost entirely replaced by biotite and iron oxides, similar to fGT. Biotite (<1 mm) occurs as brown to pale brown flakes and becomes reddish brown to pale brown towards the base of GRT with increased alteration to chlorite and iron oxides. Quartz and alkali feldspar are typically subhedral to anhedral with undulose extinction and fine perthitic exsolution, respectively. Zircon commonly appears as inclusions in biotite and quartz.

Table 2: Average composition of plagioclase from the Takidani Pluton

<i>n</i> :	Pop 1 448	Pop 2a 672	Pop 2b 442	Rim 1 29	Rim 2a 145	Rim 2b 99	Matrix 29
<i>wt %</i>							
SiO ₂	59.77 (0.81)	57.53 (1.47)	56.82 (1.48)	62.35 (1.38)	63.23 (1.58)	63.00 (1.61)	62.31 (1.06)
Al ₂ O ₃	24.66 (0.57)	26.17 (1.02)	26.89 (0.97)	23.00 (0.88)	22.57 (0.96)	22.98 (1.05)	23.07 (0.85)
FeO	0.19 (0.02)	0.26 (0.07)	0.32 (0.05)	0.17 (0.03)	0.15 (0.03)	0.18 (0.04)	0.15 (0.03)
CaO	7.09 (0.62)	8.89 (1.16)	9.57 (1.17)	5.13 (1.04)	4.50 (1.16)	4.70 (1.26)	4.96 (0.89)
Na ₂ O	7.26 (0.34)	6.16 (0.68)	5.99 (0.64)	8.49 (0.60)	8.67 (0.61)	8.78 (0.77)	8.70 (0.49)
K ₂ O	0.51 (0.25)	0.44 (0.68)	0.32 (0.13)	0.45 (0.09)	0.50 (0.15)	0.52 (0.14)	0.31 (0.09)
Total	99.49 (0.35)	99.45 (0.29)	99.91 (0.51)	99.59 (0.44)	99.61 (0.30)	100.15 (0.49)	99.49 (0.57)
<i>mol</i>							
An	0.34 (0.03)	0.43 (0.06)	0.46 (0.06)	0.24 (0.05)	0.22 (0.06)	0.22 (0.06)	0.24 (0.04)
Ab	0.63 (0.03)	0.54 (0.06)	0.52 (0.05)	0.73 (0.05)	0.76 (0.05)	0.75 (0.06)	0.75 (0.04)
Or	0.03 (0.01)	0.03 (0.04)	0.02 (0.01)	0.03 (0.01)	0.03 (0.01)	0.03 (0.01)	0.02 (0.00)
Fe × 10	0.29 (0.03)	0.41 (0.04)	0.48 (0.08)	0.25 (0.04)	0.23 (0.05)	0.26 (0.07)	0.22 (0.05)

Pop, population; *n*, sample number; An, anorthite fraction; Ab, albite fraction; Or, orthoclase fraction; values show average compositions with standard deviation (1σ) listed in parentheses.

Table 3: Average compositions of high-Al amphiboles (5.8–8.0 wt % Al₂O₃) of the Takidani pluton

	mGT (<i>n</i> = 7)	pGT (<i>n</i> = 27)	GDT (<i>n</i> = 24)	GRT (<i>n</i> = 4)
SiO ₂	46.64 (0.72)	47.15 (0.52)	47.32 (0.55)	47.47 (0.51)
TiO ₂	1.49 (0.12)	1.65 (0.10)	1.61 (0.15)	1.57 (0.23)
Al ₂ O ₃	7.12 (0.57)	6.80 (0.43)	6.58 (0.36)	6.25 (0.47)
FeO	17.17 (0.33)	15.07 (0.47)	15.36 (0.47)	14.70 (1.29)
MgO	11.71 (0.31)	13.34 (0.44)	13.32 (0.41)	13.91 (0.73)
MnO	0.70 (0.05)	0.31 (0.05)	0.36 (0.09)	0.33 (0.08)
CaO	11.11 (0.08)	11.17 (0.09)	11.14 (0.09)	11.24 (0.12)
Na ₂ O	1.52 (0.11)	1.52 (0.16)	1.46 (0.08)	1.50 (0.12)
K ₂ O	0.64 (0.09)	0.67 (0.06)	0.65 (0.06)	0.65 (0.04)
F	n.a.	n.a.	n.a.	n.a.
Cl	0.15 (0.02)	0.14 (0.02)	0.14 (0.04)	0.13 (0.04)
Total	98.24 (0.29)	97.83 (0.38)	97.95 (0.37)	97.74 (0.10)
<i>T-sites</i>				
Si	6.87 (0.09)	6.91 (0.06)	6.94 (0.06)	6.97 (0.07)
Al ^{iv}	1.13 (0.09)	1.09 (0.06)	1.06 (0.06)	1.03 (0.07)
	8.00	8.00	8.00	8.00
<i>M1–3 sites</i>				
Al ^{vi}	0.11 (0.01)	0.09 (0.03)	0.07 (0.01)	0.05 (0.01)
Ti	0.16 (0.01)	0.18 (0.01)	0.18 (0.02)	0.17 (0.03)
Fe ³⁺	0.51 (0.02)	0.44 (0.06)	0.41 (0.05)	0.30 (0.08)
Mg	2.57 (0.06)	2.91 (0.09)	2.91 (0.08)	3.04 (0.14)
Mn	0.09 (0.01)	0.04 (0.01)	0.04 (0.01)	0.04 (0.01)
Fe ²⁺	1.55 (0.05)	1.34 (0.10)	1.38 (0.07)	1.39 (0.21)
Ca	0.00 (0.00)	0.00 (0.00)	0.00 (0.00)	0.00 (0.00)
	5.00	5.00	5.00	5.00
<i>M4 site</i>				
Fe	0.05 (0.01)	0.07 (0.03)	0.09 (0.02)	0.12 (0.04)
Ca	1.75 (0.01)	1.75 (0.02)	1.75 (0.02)	1.77 (0.01)
Na	0.19 (0.01)	0.18 (0.03)	0.16 (0.03)	0.11 (0.05)
<i>A site</i>				
Ca	0.00 (0.00)	0.00 (0.00)	0.00 (0.00)	0.00 (0.00)
Na	0.24 (0.03)	0.25 (0.04)	0.26 (0.03)	0.32 (0.05)
K	0.12 (0.02)	0.13 (0.01)	0.12 (0.01)	0.12 (0.01)
Sum cations	15.36 (0.05)	15.38 (0.05)	15.38 (0.04)	15.44 (0.05)
<i>OH site</i>				
O	0.00 (0.00)	0.00 (0.00)	0.00 (0.00)	0.00 (0.00)
OH	1.96 (0.01)	1.96 (0.01)	1.96 (0.01)	1.97 (0.01)
F	0.00 (0.00)	0.00 (0.00)	0.00 (0.00)	0.00 (0.00)
Cl	0.04 (0.01)	0.04 (0.01)	0.04 (0.01)	0.03 (0.01)
Mg#	0.51 (0.01)	0.58 (0.02)	0.58 (0.02)	0.61 (0.03)

Mg#, magnesium number; n.a., not analysed.

Table 4: Modal abundances (area %) of mineral phases in GDT, pGT and mGT units obtained from QEMSCAN analyses

Unit: Sample:	GDT EH16	GDT EH23	pGT EH12	pGT EH76	pGT EH70	mGT EH5
Plagioclase feldspar	43.25	49.27	43.47	41.10	36.57	46.64
Quartz	26.07	21.44	26.52	28.52	31.13	24.12
K-feldspar	14.64	14.29	15.58	19.04	21.93	16.07
Amphibole	5.24	5.89	3.90	3.17	2.59	5.69
Biotite/phlogopite	7.71	6.00	7.59	4.95	5.67	5.28
Chlorite	0.70	1.40	0.75	1.62	0.75	0.65
Fe-oxides	0.56	0.37	0.50	0.29	0.18	0.60
Ilmenite	0.18	0.14	0.13	0.08	0.12	0.22
Apatite	0.28	0.24	0.29	0.23	0.17	0.27
Titanite	0.13	0.25	0.13	0.36	0.12	0.17
Epidote	0.27	0.12	0.26	0.16	0.12	0.02
Zircon	0.02	0.02	0.02	0.01	0.02	0.02
Kaolinite	0.00	0.00	0.00	0.02	0.00	0.12
Others	0.96	0.56	0.86	0.45	0.63	0.12

Equigranular hbl–bt–granodiorite (GDT)

The basal contact between GDT and GRT is covered by boulders and blocks and is not visible in the Shiradashi-zawa valley. The top contact with pGT can be followed in the field and is not sharp but gradual. GDT is

equigranular, medium- to coarse-grained (<10 mm; Fig. 2) and has similar textural characteristics throughout the TK. GDT contains plagioclase (43–49 area %), quartz (21–26 area %), alkali feldspar (14–15 area %), biotite (7–8 area %) and amphibole (5–6 area %; Table

Table 5: Distribution of anorthite contents (area %) in GDT, pGT and mGT created from Ca maps and EMPA analyses

Unit: Sample:	GDT EH16	GDT EH23	pGT EH12	pGT EH76	pGT EH70	mGT EH5
An _{10–30}	11.7	14.1	15.3	15.9	15.2	18.0
An _{30–50}	21.6	23.2	18.4	16.8	14.1	26.8
An _{50–70}	8.4	10.6	6.9	4.9	4.0	1.4
An _{70–90}	0.7	0.2	0.4	0.2	0.3	0.0
Total (anorthite maps)	42.5	48.1	41.0	37.8	33.6	46.2
Total (QEMSCAN maps)	43.3	49.3	43.5	41.1	36.6	46.6
<i>Normalized (anorthite maps)</i>						
An _{10–30}	27.6	29.3	37.3	42.1	45.2	39.0
An _{30–50}	50.8	48.3	44.8	44.6	42.1	58.0
An _{50–70}	19.8	22.0	16.8	12.9	11.8	3.0
An _{70–90}	1.7	0.4	1.1	0.4	0.9	0.0
<i>Normalized (plagioclase content of mineral maps)</i>						
An _{10–30}	27.1	28.6	35.2	38.7	41.5	38.6
An _{30–50}	49.9	47.2	42.3	40.9	38.6	57.4
An _{50–70}	19.5	21.5	15.9	11.8	10.8	3.0
An _{70–90}	1.7	0.4	1.0	0.4	0.8	0.0

4). Plagioclase (<10 mm) is typically euhedral and contains either a resorbed calcic or patchy zoned core, an oscillatory-zoned mantle and a darker rim. Rarely, plagioclase has overgrown partly resorbed mineral aggregates. Amphibole (<4 mm) is euhedral to subhedral, often patchy zoned and may contain various mineral inclusions (i.e. iron oxides, biotite, apatite, amphibole). Biotite (<1 mm) occurs as brown to pale brown subhedral flakes. In more altered samples, biotite is dark brown in plane-polarized light. In the lower section of GDT quartz shows undulose extinction and graphic intergrowth with alkali feldspar. Apatite and zircon are mainly included in biotite and amphibole crystals. Vermicular chlorite is sporadically present and is usually associated with quartz crystals. Allanite was found in two samples.

Porphyritic granodiorite and granite (pGT)

This unit lies structurally between GDT and mGT and is distinctly porphyritic with a predominantly fine-grained matrix (<1 mm) and plagioclase and amphibole phenocrysts (<8 mm, Fig. 2). The modal proportions of the main components vary throughout the unit with the amount of plagioclase decreasing from about 43 to 37 area % upwards (Table 4). Concurrently, quartz and alkali feldspar abundances increase from about 27 to 31 area % and from 16 to 22 area %, respectively. Amphibole (3–4 area %), biotite (6–8 area %), magnetite and apatite decrease towards the upper part of the pGT (Table 4). The matrix mainly comprises alkali feldspar, quartz and plagioclase, becoming very fine-grained (20–50 µm) towards the upper contact with the mGT.

Euhedral plagioclase phenocrysts also contain resorbed or patchy zoned cores and an oscillatory-zoned mantle. Overgrowth rims become more volumetric towards the base of the pGT. Occasionally, plagioclase cores contain large amounts of mineral inclusions (Fig. 3a). Quartz occurs as 1–2 mm long euhedral to subhedral grains and as small crystals in the groundmass, whereas alkali feldspar is abundant only in the

groundmass. Subhedral biotite (<1 mm) and sub- to euhedral amphibole (<4 mm) crystals commonly incorporate iron oxides and in the case of amphibole also biotite. Sometimes, amphibole contains resorbed plagioclase (Fig. 3b). Zircon and apatite are present as accessory phases included in biotite and amphibole and within the groundmass. Micrographic intergrowth of quartz and alkali feldspar and skeletal growth of biotite and amphibole is observed near the contact with mGT. Some biotites in samples close to mGT are rimmed by iron oxides. Vermicular chlorite and epidote are observed within a miarolitic texture (Fig. 3c). Traces of orthopyroxene are included in amphibole cores.

Marginal granodiorite (mGT)

The marginal granodiorite is located at the roof of the intrusion and it is porphyritic with predominantly plagioclase phenocrysts (<10 mm) and a fine- to medium-grained matrix (<5 mm; Fig. 2). The main components are plagioclase (47 area %), quartz (24 area %), alkali feldspar (16 area %) as well as amphibole (6 area %) and biotite (6 area %; Table 4). Plagioclase phenocrysts (<10 mm) are oscillatory zoned and overgrown by a rim of different composition. Few crystals contain resorbed cores. Quartz shows weak to strong undulose extinction and occurs as large subhedral grains (<5 mm) and as small interstitial grains (<1 mm) in the matrix. Alkali feldspar occurs only in the matrix and perthites are visible in only a few cases. Amphiboles (<3 mm) are subhedral to euhedral, predominantly patchy zoned and occasionally occur as oikocrysts including biotite, iron oxides and apatite. Biotite crystals (<2 mm) occur in brown to pale brown subhedral flakes and show alteration to chlorite and iron oxides. Many biotite grains are surrounded by small iron oxides (Fig. 3d). Apatite is common and is mainly included in biotite and amphibole. Zircon is predominantly found as inclusions in biotite (Fig. 3d), but also occurs in amphibole and quartz. Titanite and rutile are present in relatively small amounts (<0.2 area %; Table 4).

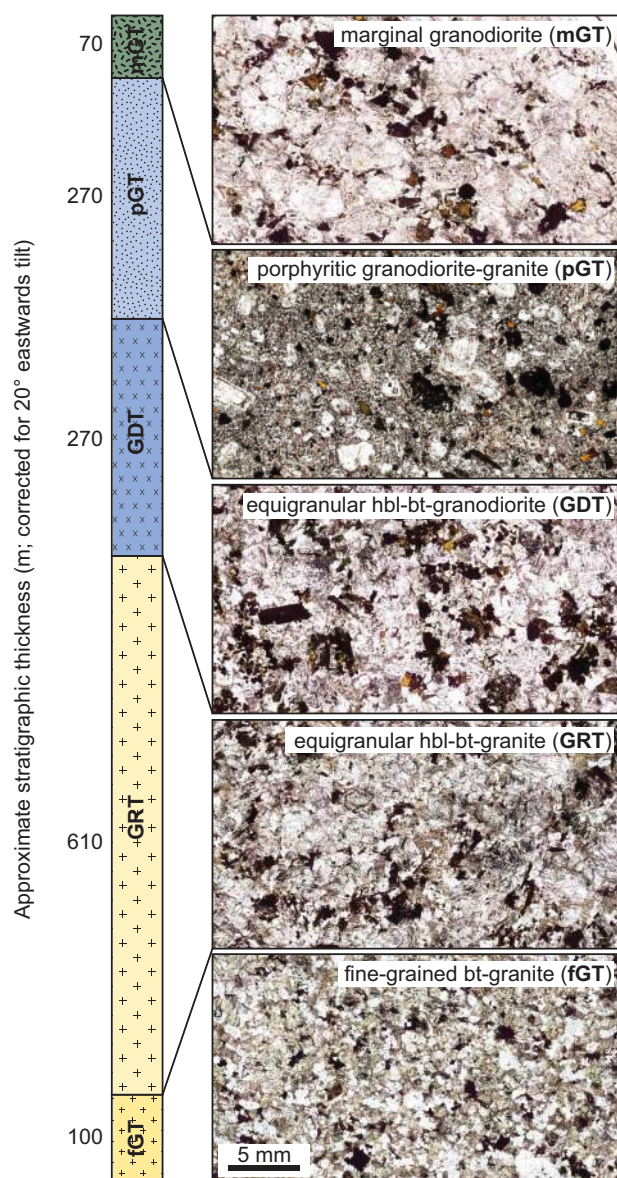


Fig. 2. Rock textures of five TK units as observed in thin section, indicating the corresponding stratigraphic locations. The basal granite (fGT) has a fine-grained equigranular texture, whereas the overlying granite (GRT) and granodiorite (GDT) are medium-grained. The porphyritic granodiorite and granite (pGT) in the upper section of the TK is distinctly porphyritic and dominated by a fine-grained groundmass. The marginal granodiorite (mGT) at the roof contact is also porphyritic, but phenocryst-dominated. Stratigraphic heights have been corrected for pluton tilting and show the estimated thickness of the various units along the Shiradashi-zawa valley.

BULK-ROCK GEOCHEMISTRY

Major and trace elements

The rocks of the TK are calc-alkaline, high in potassium and predominantly metaluminous (Fig. 4). GDT represents the least evolved unit of the TK with a silica content of 65–67 wt % SiO_2 (anhydrous). GRT and mGT are slightly more evolved (67 and 68 wt % SiO_2). The pGT unit has a more evolved composition with up to 71 wt % SiO_2 in the Shiradashi-zawa valley. fGT is the most silicic unit of the TK (73 wt % SiO_2).

Incompatible elements such as K_2O noticeably increase with SiO_2 content (Fig. 4b). Striking, however, is the sigmoidal variation of major and trace element concentrations from the bottom to the roof of the intrusion (Fig. 5; Table 1). The concentration of SiO_2 , K_2O , Rb, and Th first decrease above the base, up to about 1800 m then increase to about 2050 m, and finally decrease towards the roof of the pluton at an elevation of about 2200 m (Fig. 5). All other major and minor elements show opposite trends. It is noticeable that the concentrations of all elements are similar for GRT and mGT units.

Isotope geochemistry

All isotope values are corrected for fractionation and an age of 1.5 Ma (Sano *et al.*, 2002). The TK shows an isotopic signature characteristic for the Hida Mountain Granites with $^{87}\text{Sr}/^{86}\text{Sr}$ of 0.707061–0.707517 and $^{143}\text{Nd}/^{144}\text{Nd}$ of 0.512583–0.512462 (Fig. 6a; Table 1). The Sr-isotope ratios of the TK generally increase towards the roof, similar to observations from the Bushveld intrusion (Sharpe, 1985). The Sr, Nd and Pb isotopic compositions of GDT and pGT plot along continuous trends between the more primitive GRT and more radiogenic mGT (Fig. 6a and b; Table 1). A more substantial spread is observed in the $^{206}\text{Pb}/^{204}\text{Pb}$ (18.391–18.404) and $^{207}\text{Pb}/^{204}\text{Pb}$ (15.613–15.625) isotopic ratios.

MINERAL CHEMISTRY

Plagioclase

Plagioclase is the main mineral phase of the TK. Most phenocrysts contain resorbed cores of different size, texture and chemistry (Figs 7–9; Table 2), with an oscillatory-zoned mantle of andesine composition (An_{30-40}), and sodic rims of different thickness, with anorthite contents decreasing down to about 20 mol %. Anorthite and Fe contents of the oscillatory-zoned mantle were used to separate plagioclase into three main populations (Figs 7 and 8). Population 1 (P1) is characterized by reverse zoning with anorthite content increasing progressively from about 30 to 40 mol % and a rapid drop to 20 mol % in the outer rim. An-rich cores (>60 mol %) are sporadically observed in this population (Fig. 7a). Iron contents in plagioclase vary only slightly between 0.025 and 0.03 mol % and co-vary with anorthite content. The anorthite contents of populations 2 (P2) and 3 (P3) are generally higher than those of P1 and typically vary between 40 and 50 mol % (Fig. 7b and c). P2 and P3 are separated on the basis of the lower FeO content of the plagioclase in P2 (0.035–0.045 mol %) than in P3 (0.045–0.055 mol %).

QEMSCAN[®] and EMPA analyses (42 traverses) were used to investigate the distribution of plagioclase populations across the different units (Fig. 9; Tables 5 and 6; Supplementary Data Appendix D). Anorthite distribution maps can be used to distinguish P1 from P2 and P3 (Fig. 9). However, P2 and P3 are indistinguishable in

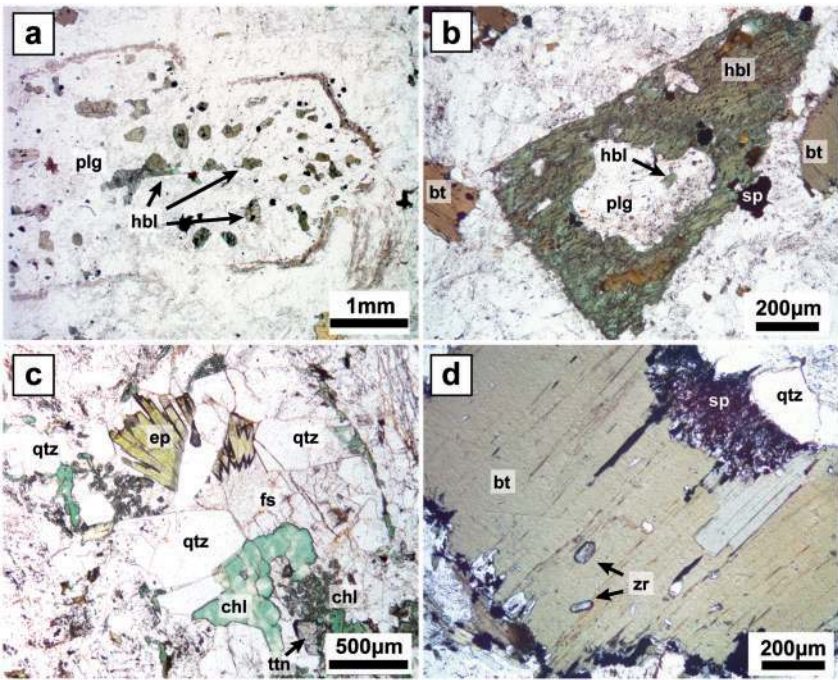


Fig. 3. Petrography of the TK rocks: (a) rare plagioclase phenocrysts containing numerous mineral inclusions including amphibole; (b) resorbed plagioclase inclusion in amphibole phenocryst in pGT; (c) miarolitic cavities in pGT containing quartz, alkali feldspar, epidote, and spherulitic and vermicular chlorite; (d) crystallization of Fe-Ti oxides along biotite rims in mGT.

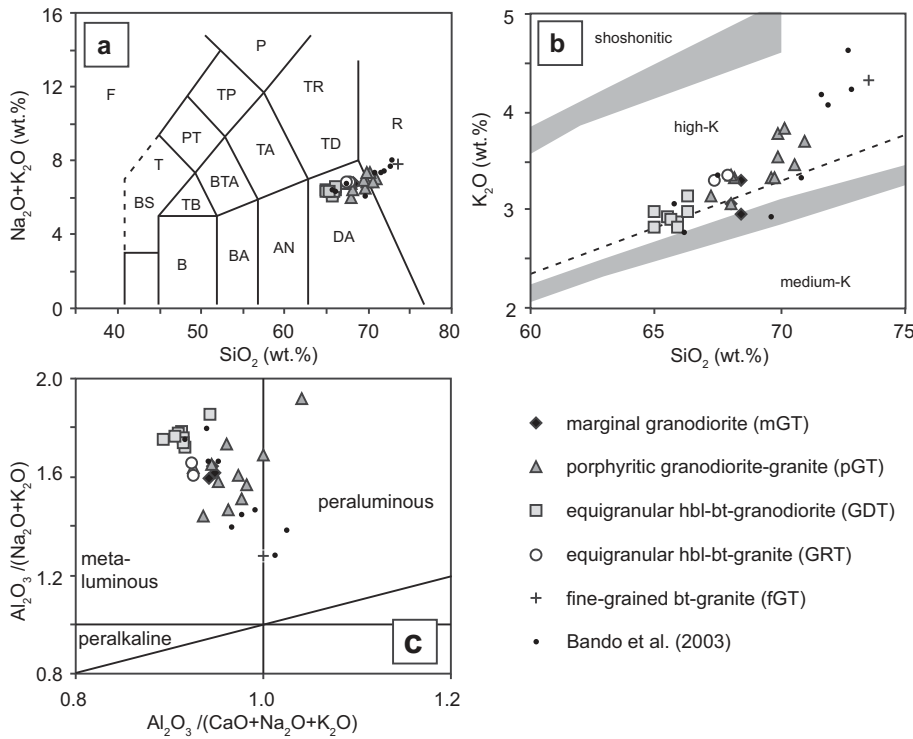


Fig. 4. Chemical classification of samples from the TK after [Le Maitre et al. \(1989\)](#). The rocks from Shiradashi-zawa are plotted together with the rock compositions of [Bando et al. \(2003\)](#). The TK samples are predominantly calc-alkaline (a), high-K (b), metaluminous rocks (c) of dacitic (i.e. granodioritic) to rhyolitic (i.e. granitic) composition.

An-maps and can be distinguished only through quantitative analyses (e.g. FeO content). No An-rich cores ([Fig. 9](#)) are observed in mGT plagioclase, whereas GDT and pGT plagioclase contains up to 2 area % ([Fig. 9](#);

[Table 5](#)). QEMSCAN and EMPA data both show that mGT contains only P1. EMPA analyses reveal that P2 is common in the GDT and pGT units (70–91%). P3 is the dominant population in GRT. Importantly, P1 is found in

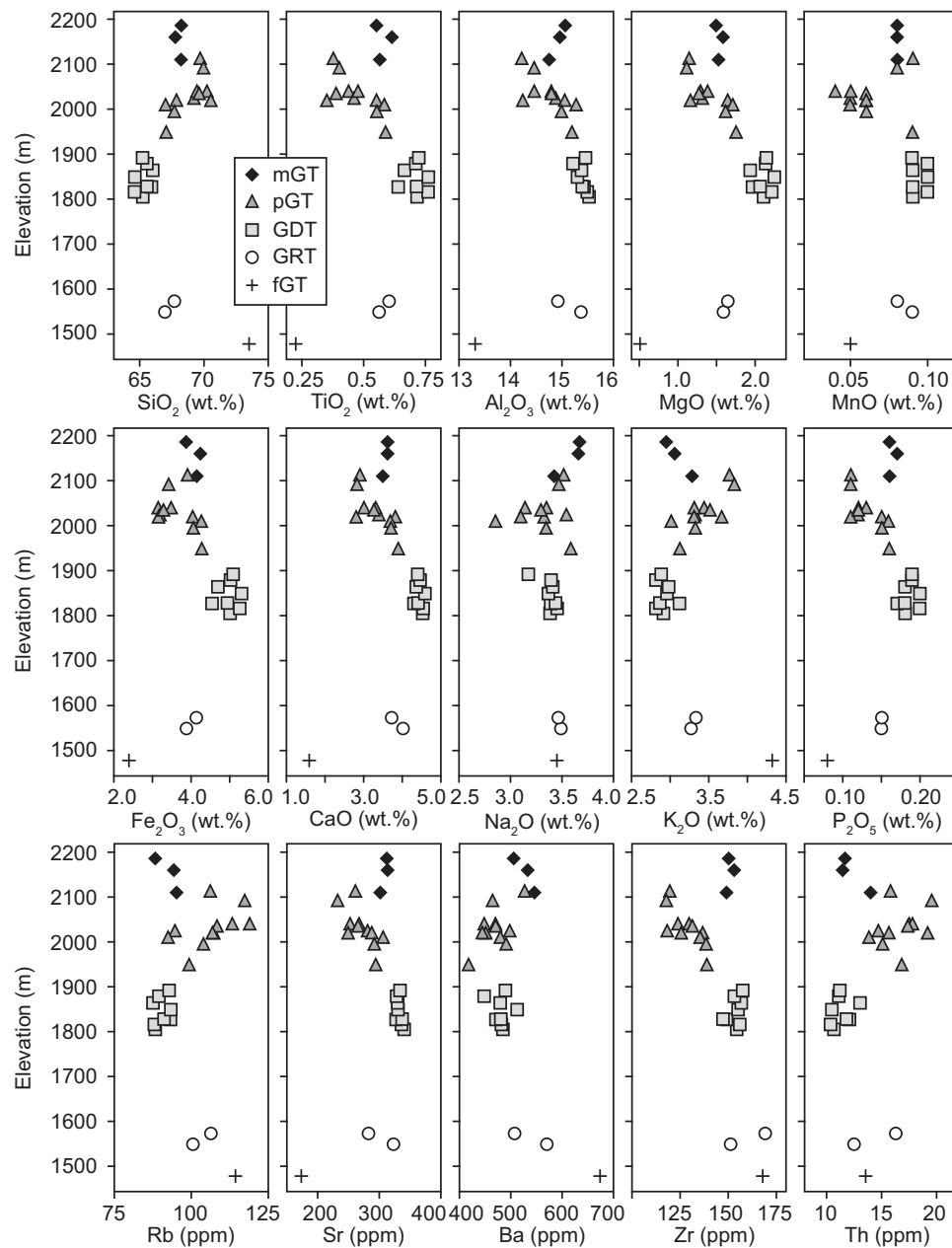


Fig. 5. Chemical variations from the base to the roof of the intrusion along the Shiradashi-zawa valley. Samples from the lower section (below 1900 m) were collected along the river. The upper part of this section (above 1900 m) was sampled along a hiking trail. Sigmoidal variations are observed from the bottom to the top of the pluton. No outcrops were observed between sample locations 15 (GRT) and 16 (GDT) (see Fig. 1). Sample 36 was collected near the road, south of Shiradashi-zawa valley. Data points are projected onto a bottom-to-top profile against the topographic altitude. No correction for the tilting of the pluton has been applied.

pGT (24%) but does not occur in either GDT or GRT. P3 is also present to small amounts in pGT (6%) and GDT (9%) units (Table 6).

Amphibole

We recalculated all amphibole compositions based on 23 oxygens, using the formula of Holland & Blundy (1994; Table 3). To obtain $\text{Fe}^{3+}/(\text{Fe}^{2+} + \text{Fe}^{3+})$ ratios, an average factor (f_{av}) was computed after Holland & Blundy (1994), who extended the criteria for elemental site occupancy of Robinson *et al.* (1982) and Spear &

Kimball (1984). Based on the calculated stoichiometry, all amphiboles can be classified as magnesio-hornblendes (Fig. 10a; Leake *et al.*, 1997), with the exception of a few high-Si crystals, which classify as actinolite.

Amphibole shows moderate compositional variation across the Takidani pluton with two distinct populations (Fig. 10b). Based on their aluminium contents, we classify these populations into low-Al ($\text{Al}_2\text{O}_3 < 5.8 \text{ wt } \%$; $\text{Al}_{\text{total}} < 1.0 \text{ a.p.f.u.}$; Supplementary Data Appendix B) and high-Al amphibole-types ($\text{Al}_2\text{O}_3 > 5.8 \text{ wt } \%$; $\text{Al}_{\text{total}} > 1.0 \text{ a.p.f.u.}$; Table 3). Most crystals display chemically distinct patchy zones (Fig. 11a and b); very few

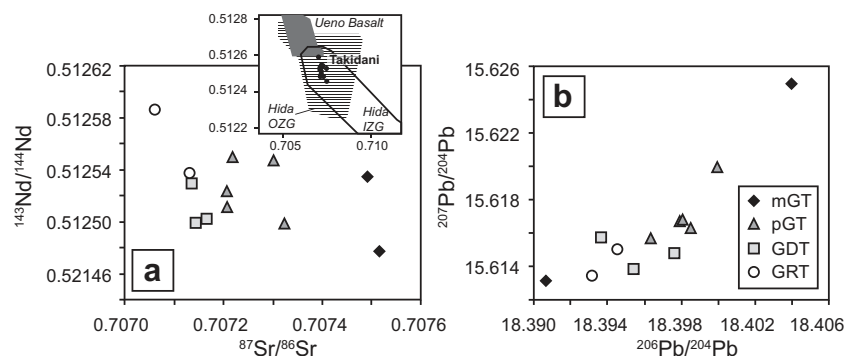


Fig. 6. (a) Variation of $^{143}\text{Nd}/^{144}\text{Nd}$ vs $^{87}\text{Sr}/^{86}\text{Sr}$ for whole-rock samples from the TK. Sr-isotope compositions become more radiogenic roofwards from GRT to mGT. The samples have a typical signature of Hida outer zone granites (OZG) and inner zone granites (IZG) (Kimura & Nagahashi, 2007). (b) Variation of $^{207}\text{Pb}/^{204}\text{Pb}$ vs $^{206}\text{Pb}/^{204}\text{Pb}$ for whole-rock samples from the TK. Pb isotope compositions generally increase roofwards from GRT to mGT. The samples of the mGT unit show a large spread in Pb isotope ratios. All values are corrected for an age of 1.5 Ma.

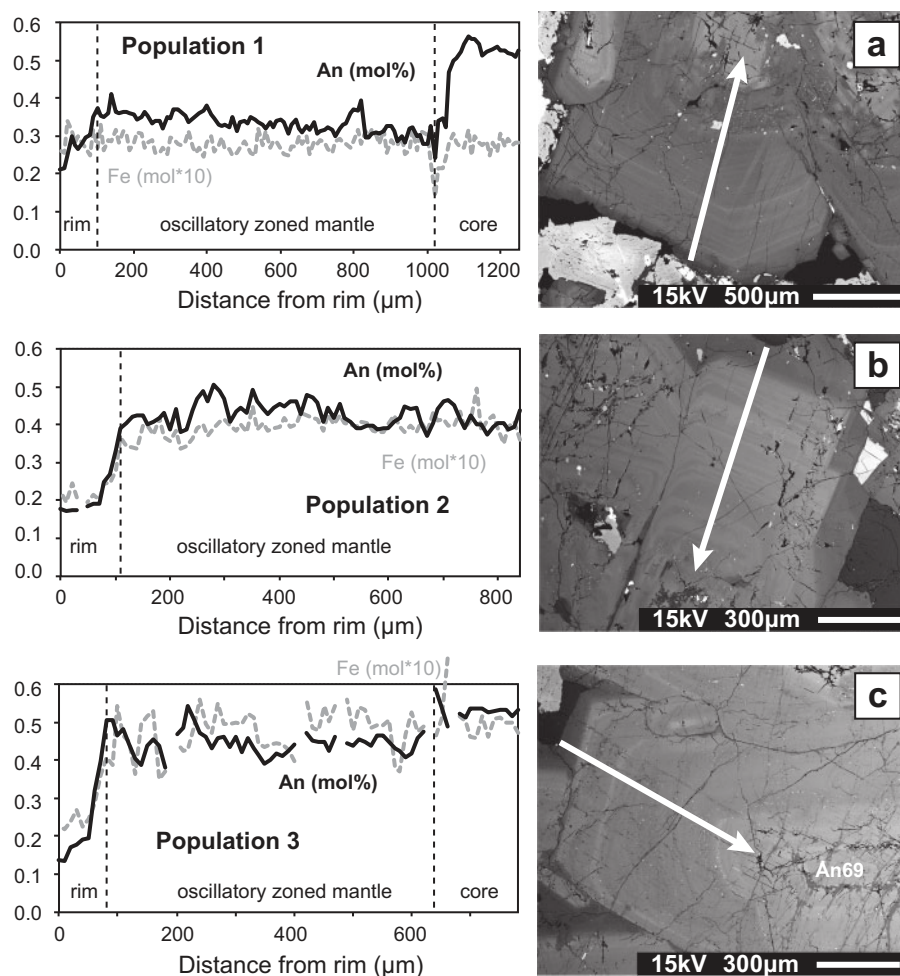


Fig. 7. Electron microprobe profiles (10 μm steps) of examples of the three plagioclase populations. Each population is defined by the anorthite and iron content of the oscillatory-zoned mantle of each crystal. Population 1 is reversely zoned from about 30 to 40 mol % anorthite (a). Populations 2 and 3 have similar An contents, varying between about 40 and 50 mol %, but distinctively different iron concentrations (b, c).

crystals have rounded amphibole cores or contain amphibole grains with Al_2O_3 content above 8 wt % (Fig. 11c and d). Back-scattered electron (BSE) images of amphibole grains show that brighter zones are higher in Al than darker ones (Fig. 11b).

Biotite

Biotite is invariably interstitial and anhedral (with the exception of pGT), suggesting its late appearance in the crystallization sequence. Chemical compositions vary only slightly and without any obvious trends between

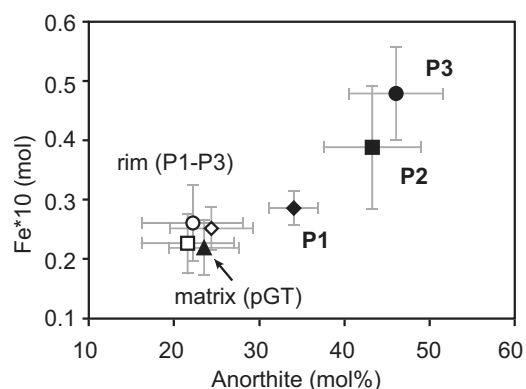


Fig. 8. Variations of Fe and An contents of plagioclase populations (i.e. oscillatory-zoned mantle) from 42 plagioclase traverses of the TK. Analyses of rim plagioclases (white fill) and matrix plagioclases of pGT (black triangle) have similar chemistry. Errors are given as 1σ .

the units (Supplementary Data Appendix C). However, concentrations of Mn (Fig. 12a) and Cl (Fig. 12b) plotted against biotite magnesium-number (Mg#) seem to outline different populations. The concentration of Mn in biotite tends to increase towards the roof of the intrusion (from GRT to pGT), whereas the concentration of Cl in biotite generally decreases roofwards from 0.48 to 0.35 wt %.

Oxides

Titano-magnetite is the dominant oxide phase in Takidani samples (Supplementary Data Appendix D). Ilmenite is also present and is usually associated with magnetite, forming exsolution lamellae or single grains. The compositions of the Fe–Ti oxides are generally homogeneous across the pluton (Supplementary Data Appendix D); however, a relatively minor increase of

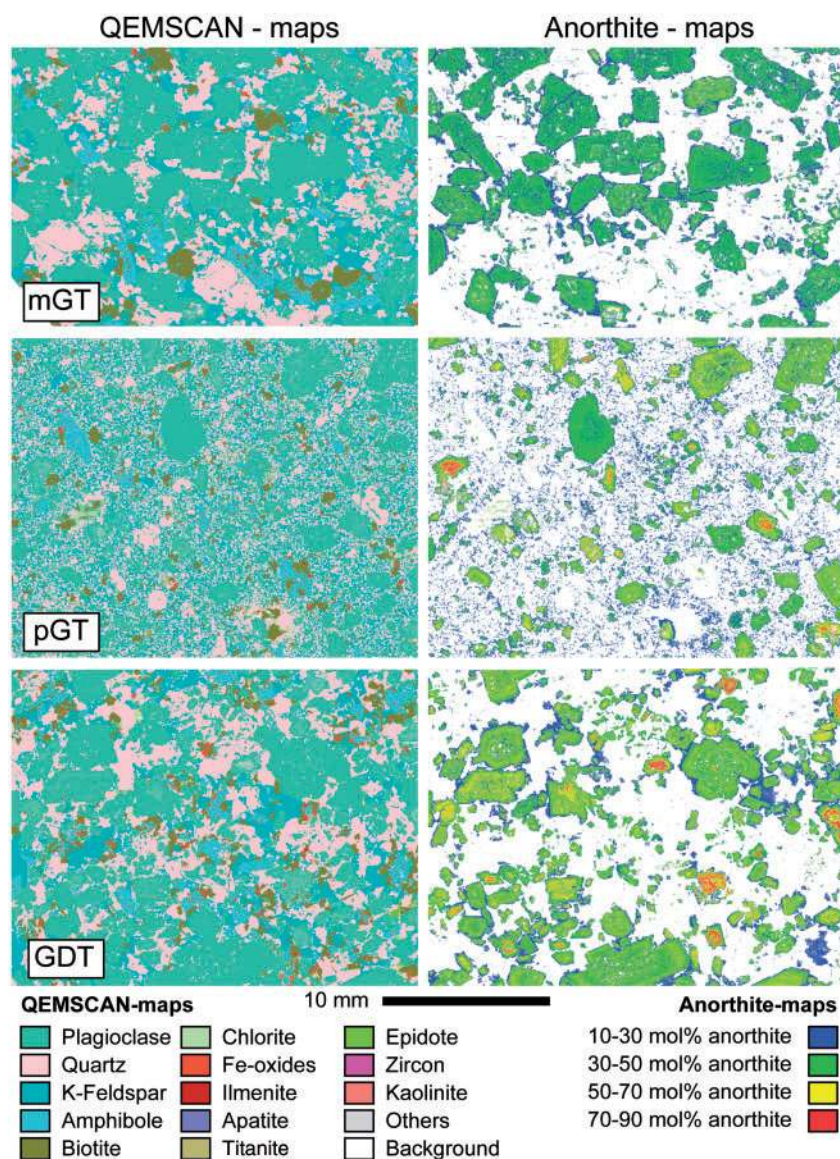


Fig. 9. QEMSCAN[®] and anorthite maps of the GDT, pGT and mGT units. Anorthite maps are calibrated with electron microprobe data to define anorthite bins of 20 mol %.

Table 6: Abundance of plagioclase populations (%) across the Takidani Pluton

Population:		P1	P2	P3
mGT	<i>n</i> = 6	100	—	—
pGT	<i>n</i> = 17	24	70	6
GDT	<i>n</i> = 11	—	91	9
GRT	<i>n</i> = 8	—	—	100
fGT	<i>n.a.</i>	<i>n.a.</i>	<i>n.a.</i>	<i>n.a.</i>

EMPA analyses of 42 plagioclase traverses; *n.a.*, not applicable.

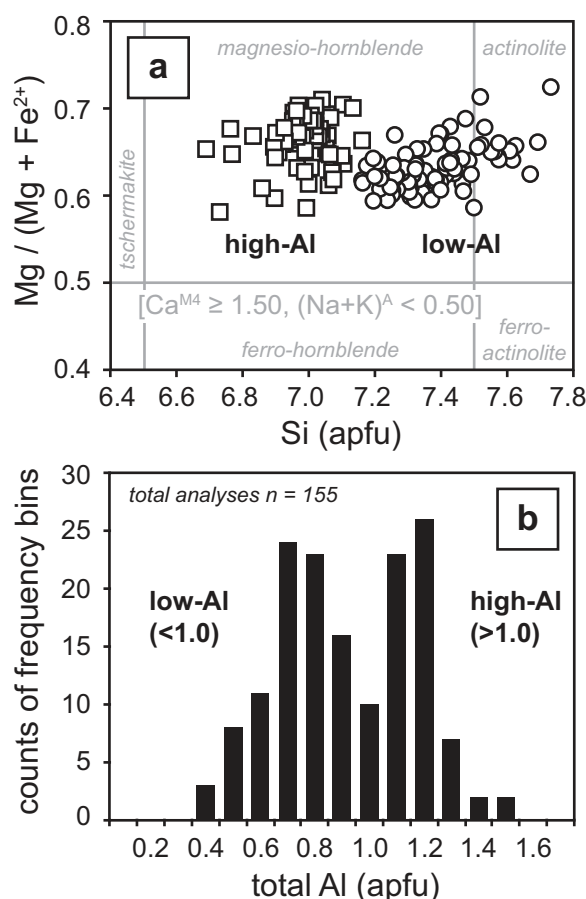


Fig. 10. Amphibole classification (a) and subdivision of amphiboles based on total Al a.p.f.u. (b). Stoichiometry is recalculated after Holland & Blundy (1994) and plotted using the classification scheme of Leake *et al.* (1997). Most amphiboles classify as magnesio-hornblende with the exception of a few amphibole rims, which fall into the actinolite field. The total Al (in a.p.f.u.) values show a bimodal distribution with low-Al (<1.0 total Al a.p.f.u.; Supplementary Data Appendix B) and high-Al (>1.0 total Al a.p.f.u.; Table 3) amphibole populations.

MnO content in ilmenite follows the same increasing trend observed for MnO content in biotite and low-Al amphiboles.

Barometry and thermometry

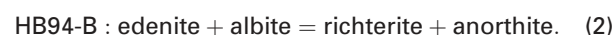
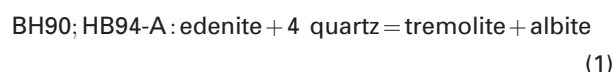
The Al-in-hornblende geobarometer of Anderson & Smith (1995) is calibrated using data from Johnson & Rutherford (1989) and Schmidt (1992), and can be used

to estimate the crystallization pressure, P (in kbar), of hornblende, based on the total aluminium content (in atoms per formula unit, or a.p.f.u.), provided that the crystallization temperature, T ($^{\circ}\text{C}$), is independently known:

$$P(\pm 0.6 \text{ kbar}) = 4.76 \text{ Al} - 3.01$$

$$- \{ [T(^{\circ}\text{C}) - 675] / 85 \{ 0.530 \text{ Al} + 0.005294 [T(^{\circ}\text{C}) - 675] \} \}.$$

Temperature estimates can be derived from the pressure-dependent plagioclase–hornblende thermometers of Blundy & Holland (1990; BH90) and Holland & Blundy (1994; HB94-A and HB94-B) using the following two equilibria:



The first equilibrium reaction is used for BH90 and HB94-A thermometers and requires silica-saturation. BH90 is based on a more restricted experimental dataset of igneous rock suites, considering only ideal interactions in amphibole. The HB94 model is extended to a wider dataset of igneous and metamorphic rocks to account for non-ideal interactions in amphiboles and includes an improved hornblende formulation to estimate ferric iron contents, optimized for the HB94 thermometers. A comparison of different thermometers (Anderson, 1996; Bachmann & Dungan, 2002) shows that the edenite–richterite thermometer of HB94 [equation (2)] in combination with the Al-in-hornblende barometer of Anderson & Smith (1995) produces the most reliable temperature solutions for plutonic and volcanic rocks at or near the granitic to tonalitic solidi (Anderson *et al.*, 2008).

Fe-rich hornblendes may not be suitable to use in geobarometry, depending on the amount of ferric iron. Anderson & Smith (1995) noted that $\text{Fe}^{3+}/(\text{Fe}^{3+} + \text{Fe}^{2+})$ ratios that are lower than 0.25 for amphiboles recalculated after Leake *et al.* (1997) should not be used for their Al-in-hornblende barometer. Because Holland & Blundy (1994) used a different method to calculate $\text{Fe}^{3+}/\text{Fe}^{2+}$, we first recalculated the stoichiometric formula for amphiboles using the method of Leake *et al.* (1997) and excluded analyses with $\text{Fe}^{3+}/(\text{Fe}^{3+} + \text{Fe}^{2+})$ ratios lower than 0.25; then we recalculated the cation occupancies in amphibole after Holland & Blundy (1994) to apply their thermometer.

DISCUSSION

Reconstructing the plumbing system of Takidani

A comparison between natural samples and experiments performed at different pressures, temperatures and water activities has the potential to estimate ranges of crystallization depth and temperature, therefore providing information about the architecture of magmatic plumbing systems.

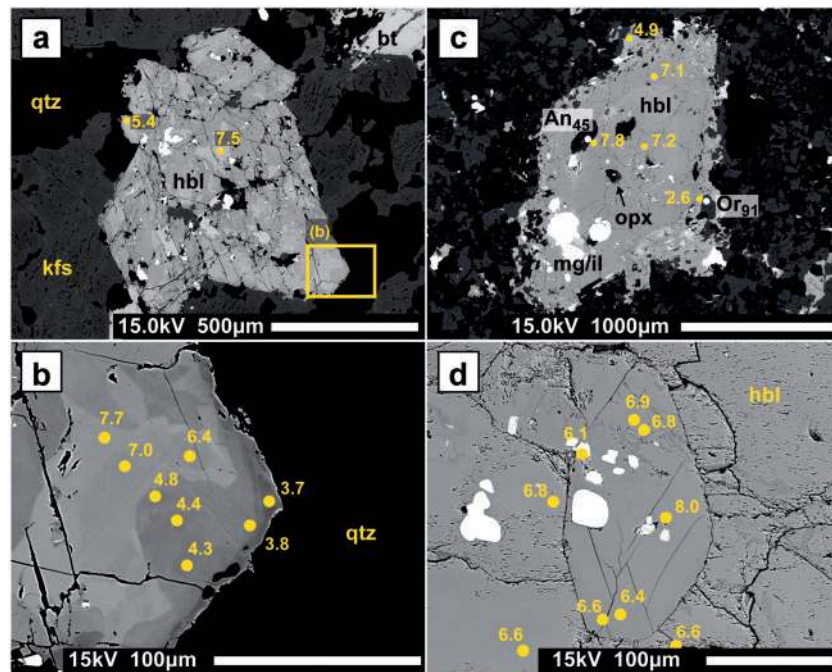


Fig. 11. Back-scattered electron (BSE) images of selected amphibole grains including Al_2O_3 contents (in wt %) of electron microprobe spot analyses. (a) Patchy zoned amphibole in mGT. (b) Patchy zoning in amphibole with Al_2O_3 varying from 7.7 wt % in the bright zone to 3.7 wt % in the darker coloured rim. (c) Amphibole in pGT contains plagioclase with 45 mol % anorthite along a rounded crystal core. The interstitially grown crystal rim contains less than 5 wt % Al_2O_3 . (d) Amphibole inclusion with Al_2O_3 content up to 8 wt %.

Previous estimates of emplacement depth and temperature for the TK were based on the Al-in-hornblende geobarometer of Anderson & Smith (1995) and the thermometer of Blundy & Holland (1990). The derived average emplacement pressure was about 250 MPa (± 60 MPa) with slightly lower estimates for the emplacement pressure in the Shiradashi-zawa valley (222 MPa; Bando *et al.*, 2003). Calculations performed using samples collected in different portions of the pluton indicate an increase of emplacement pressure from 165 MPa at the base to 250 MPa at the roof of the intrusion. The progressive decrease of emplacement depth from about 9.5 km to 6.5 km has been previously explained by unroofing during emplacement of the pluton by under-accretion (Bando *et al.*, 2003). Bando *et al.* (2003) estimated the magma temperature during intrusion at 710°C. In this study we reassess the emplacement conditions of the TK using the high spatial resolution sampling performed in our study and applying the geothermometers of Holland & Blundy (1994). We further compare the whole-rock chemistry and mineral chemistry of our samples with phase equilibria experiments performed at various pressures, temperatures and water contents with starting material of composition similar to the rocks we have studied (Whitney, 1975, 1988; Sisson & Grove, 1993; Scaillet & Evans, 1999; Costa *et al.*, 2004; Holtz *et al.*, 2005; Arce *et al.*, 2013; Caricchi & Blundy, 2015).

Experimental studies have shown that temperature and pressure have an effect on amphibole compositions as a result of atomic exchange reactions (Spear,

1981; Johnson & Rutherford, 1989; Blundy & Holland, 1990; Thomas & Ernst, 1990; Schmidt, 1992). An increase in pressure leads to the replacement of Mg by Al in the octahedral M-sites (Al-Tschermak substitution; $\text{Si}^{\text{T}} + \text{Mg}^{\text{M1-M3}} = \text{Al}^{\text{T}} + \text{Al}^{\text{M1-M3}}$), whereas an increase in temperature causes Ti to replace Mn in the octahedral M-sites (Ti-Tschermak substitution; $2\text{Si}^{\text{T}} + \text{Mn}^{\text{M1-M3}} = 2\text{Al}^{\text{T}} + \text{Ti}^{\text{M1-M3}}$) and causes Na and K to occupy the A-sites [edenite exchange; $\text{Si}^{\text{T}} + \square^{\text{A1}} = \text{Al}^{\text{T}} + (\text{Na} + \text{K})^{\text{A}}$]. In all three cases, Al substitutes for Si in the tetrahedral T-sites.

The TK hornblendes show a range of Al^{T} between 0.3 and 1.4 a.p.f.u. that correlates positively with the edenite $[(\text{Na} + \text{K})^{\text{A}}]$ (Fig. 13a), Ti-Tschermak ($\text{Ti}^{\text{M1-M3}}$; Fig. 13b) and Al-Tschermak ($\text{Al}^{\text{M1-M3}}$; Fig. 13c) components throughout the various units constituting the TK. Edenite and Ti-Tschermak exchange reactions are estimated from regression slopes (Shane & Smith, 2013) and account for about 21% and 34% respectively of the total Al variability, whereas the Al-exchange reaction accounts for only about 7%. The plagioclase exchange reaction on the larger M4 site ($\text{Si}^{\text{T}} + \text{Na}^{\text{M4}} = \text{Al}^{\text{T}} + \text{Ca}^{\text{M4}}$) also appears to play a significant role in the Takidani amphiboles (Fig. 13d). The rather poor correlation between Ca^{M4} and Al^{IV} is probably caused by differences in the An-Ab components of the co-crystallizing plagioclase. Whereas the majority of amphibole analyses above 0.65 Al (a.p.f.u.) show a positive correlation between Ca^{M4} and Al^{IV} , the correlation is negative (-0.094) for amphiboles from mGT (0.5–1.2 Al a.p.f.u.). Such negative correlation, together with the reverse zoning in

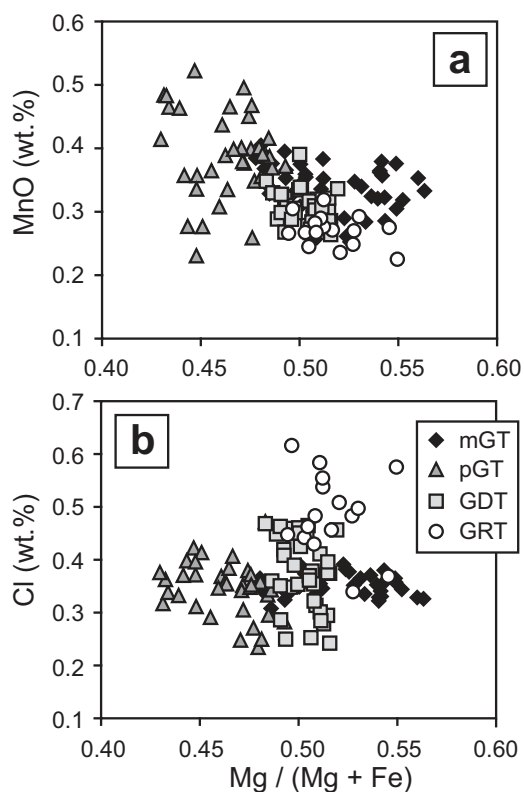


Fig. 12. (a) Variation of MnO vs Mg/(Mg + Fe) for biotite from TK lithological units. Biotite grains from the fine-grained pGT unit have generally lower magnesium contents than in all other units, indicating that they crystallized from potentially more evolved melts. (b) Variation of Cl vs Mg/(Mg + Fe) for biotite from the TK. Cl contents can be used to separate biotite of GRT and mGT into two distinct groups. The highest Cl contents in biotite are found in GRT at the base of the TK.

P1 of mGT, was possibly caused by the input of mafic magma.

Plagioclase–hornblende pairs

Subhedral plagioclase with anorthite content of 40–45 mol % is occasionally included in high-Al amphiboles with Al_2O_3 close to or above 8 wt %. Amphibole oikocrysts occasionally contain small plagioclase (An_{30}) or alkali feldspar inclusions. The majority of amphibole grains are associated with apatite, Fe–Ti oxides and biotite. Amphibole crystals also tend to be much smaller than plagioclase phenocrysts and therefore have most probably formed after the crystallization of the plagioclase phenocrysts ($<\text{An}_{40}$; Figs 8 and 9). A rapid decrease from An_{40} to An_{30} is observed in the plagioclase rims, indicating either chemical evolution of the residual melt during progressive cooling or a decrease in water activity (Riker *et al.*, 2015) caused by the introduction of CO_2 from depth (Newman & Lowenstern, 2002; Papale & Barbato, 2006). All plagioclase phenocrysts share the same late-stage evolution of the outer rim chemistry, which suggests that the Na-rich overgrowth was formed when the magma achieved a mush state with a crystallinity above 40–50 vol. % (Hildreth, 1981; Marsh, 1981).

Given the difficulty of finding enough amphibole–plagioclase pairs in direct contact to apply the Blundy & Holland (1990) and Holland & Blundy (1994) thermometers in a meaningful way, we considered a range of anorthite contents of the plagioclase in equilibrium with amphibole of 30–45 mol %. These estimates are based on the composition of plagioclase inclusions found in

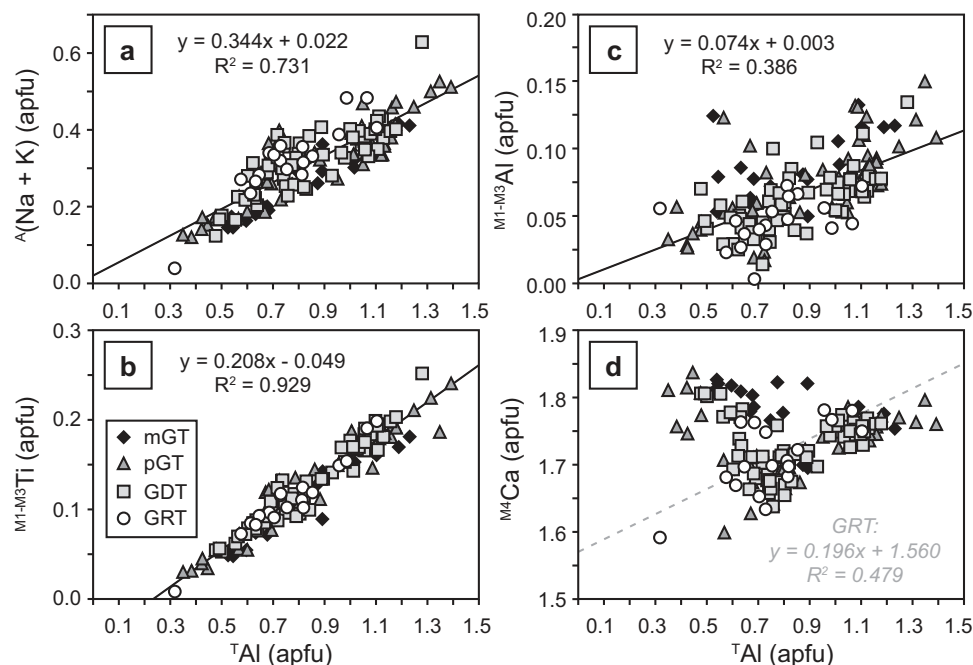


Fig. 13. Amphibole substitutions: (a) temperature-dependent Ti-Tschermak exchange; (b) temperature-dependent edenite exchange; (c) pressure-dependent Al-Tschermak exchange; (d) plagioclase-dependent Ca exchange. Slopes are calculated using all the data with the exception of the Ca-exchange reaction, where the slope is calculated based on the analyses of GRT only.

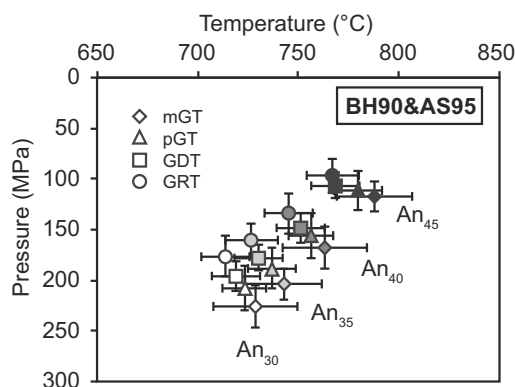


Fig. 14. Mean temperature and pressure estimates with 1 σ error bars for high-Al amphiboles using the Blundy & Holland (1990) thermometer and Anderson & Smith (1995) barometer. Results are shown for a range of An contents varying from 30 to 45 mol %.

amphiboles. Additionally, matrix plagioclase in pGT has a maximum anorthite content of 30 mol %, suggesting that amphibole crystallized before the matrix plagioclase. Calculated mean temperatures for Shiradashizawa samples (Supplementary Data Appendix F) vary from 673°C ($\pm 28^\circ\text{C}$) to 700°C ($\pm 33^\circ\text{C}$) using anorthite contents of 30 mol %. Mean values increase from temperatures of 715°C ($\pm 35^\circ\text{C}$) to 750°C ($\pm 42^\circ\text{C}$) using anorthite contents of 45 mol %. Our pressure estimates are somewhat lower than those determined by Bando *et al.* (2003), with average pressures between 99 MPa (± 59 MPa) and 161 MPa (± 67 MPa) using 30 mol % anorthite (Supplementary Data Appendix F), and between 63 MPa (± 33 MPa) and 92 MPa (± 32 MPa) using 45 mol % anorthite (Supplementary Data Appendix F).

To constrain better the crystallization conditions of the TK we considered the two main amphibole populations [low-Al (3.6–5.8 wt % Al_2O_3) and high-Al (5.8–8.0 wt % Al_2O_3)] individually. Overall, the average temperature ranges between 714°C ($\pm 12^\circ\text{C}$) and 788°C ($\pm 24^\circ\text{C}$) for high-Al amphiboles and between 654°C ($\pm 24^\circ\text{C}$) and 700°C ($\pm 18^\circ\text{C}$) for low-Al amphiboles (Fig. 14; Supplementary Data Appendix G). Recalculated crystallization pressures are also distinctively higher for high-Al versus low-Al amphibole populations (Supplementary Data Appendix G). Pressures determined for high-Al amphibole show a general increase of crystallization pressure towards the roof from about 97 MPa (± 6 MPa) to 226 MPa (± 21 MPa), in general agreement with Bando *et al.* (2003). Calculations with low-Al amphiboles yield relatively homogeneous crystallization pressures of 52–82 MPa across the entire pluton (Supplementary Data Appendix G). Considering a range of An contents, our pressure estimates (P) correspond to a crystallization depth, h [$h = P/(g\rho)$], of 3.5–8.5 km for high-Al amphiboles, and of 2.0–3.0 km for low-Al amphiboles, applying an average crustal density (ρ) of 2700 kg m $^{-3}$.

Importantly, low-Al amphiboles are generally observed as patchy zones and may indicate magma oxidation and near- or sub-solidus alteration (Hammarstrom

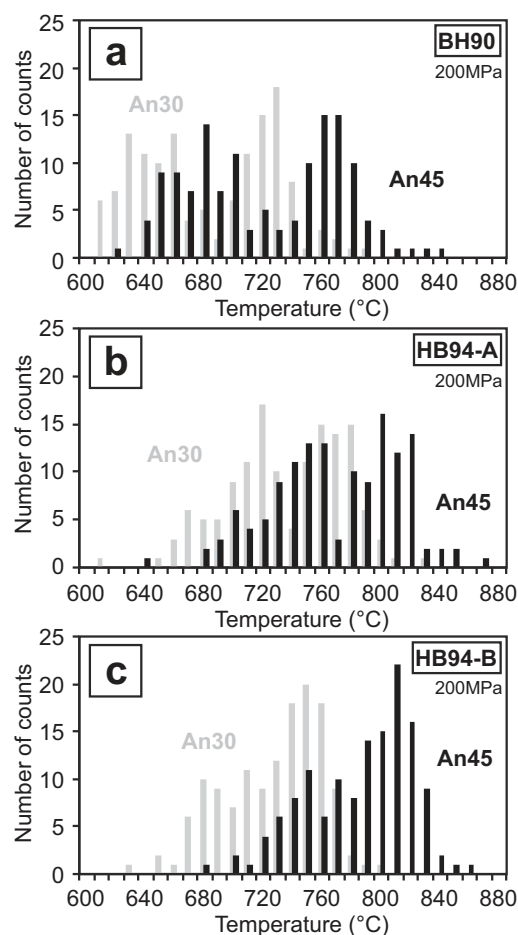


Fig. 15. Temperature distribution for TK amphiboles at 200 MPa using the thermometers of Blundy & Holland [1990; BH90 (a)] and Holland & Blundy [1994; HB94-A (b) and HB94-B (c)]. Temperatures are calculated for An contents of 30 mol % (grey) and 45 mol % (black).

& Zen, 1986; Kawakatsu & Yamaguchi, 1987; Martin, 2007). Therefore, both amphibole populations could have formed under near-isobaric conditions and the difference in Al may be related to the temperature and chemical variability of the residual melt from which they crystallized, more than pressure, as also suggested by the calculated exchange reactions (Fig. 13; Spear, 1981; Blundy & Holland, 1990; Scaillet & Evans, 1999; Bachmann & Dungan, 2002; Costa *et al.*, 2004).

Considering that pressure appears to have a secondary effect in controlling the chemical variability of amphibole, we consider isobaric crystallization and recalculate temperatures at 200 MPa. Under this assumption high-Al amphiboles yield crystallization temperatures of 766–810°C for HB94-A, 733–814°C for HB94-B and 711–776°C for BH90 (Fig. 15; Table 7), temperatures significantly higher than those estimated by Bando *et al.* (2003). Temperature estimates for low-Al amphiboles range between 686 and 742°C for HB94-A, between 685 and 771°C for HB94-B and between 638 and 681°C for BH90 (Table 7). The results from the BH90 thermometer yield values lower than temperature

Table 7: Temperature evaluation (°C) at 200 MPa for low-Al and high-Al amphibole populations

Unit:		mGT	pGT	GDT	GRT
<i>Holland & Blundy (1994), equation (1)</i>					
low-Al	An ₃₀	686 (±37)	709 (±24)	709 (±20)	712 (±16)
low-Al	An ₃₅	693 (±38)	717 (±25)	717 (±21)	719 (±16)
low-Al	An ₄₀	703 (±39)	728 (±26)	727 (±22)	730 (±17)
low-Al	An ₄₅	714 (±40)	740 (±27)	739 (±22)	742 (±17)
high-Al	An ₃₀	766 (±18)	767 (±15)	767 (±15)	773 (±12)
high-Al	An ₃₅	775 (±18)	777 (±16)	777 (±15)	782 (±13)
high-Al	An ₄₀	788 (±19)	789 (±16)	789 (±16)	795 (±13)
high-Al	An ₄₅	802 (±20)	803 (±17)	803 (±16)	810 (±14)
<i>Holland & Blundy (1994), equation (2)</i>					
low-Al	An ₃₀	694 (±18)	712 (±24)	699 (±26)	685 (±55)
low-Al	An ₃₅	712 (±18)	731 (±25)	717 (±27)	703 (±57)
low-Al	An ₄₀	731 (±18)	751 (±26)	736 (±28)	722 (±59)
low-Al	An ₄₅	750 (±18)	771 (±27)	755 (±30)	740 (±61)
high-Al	An ₃₀	754 (±9)	754 (±11)	749 (±8)	733 (±21)
high-Al	An ₃₅	774 (±9)	773 (±11)	769 (±9)	751 (±22)
high-Al	An ₄₀	794 (±9)	794 (±11)	789 (±9)	771 (±23)
high-Al	An ₄₅	814 (±9)	814 (±12)	808 (±9)	790 (±24)
<i>Blundy & Holland (1990)</i>					
low-Al	An ₃₀	638 (±29)	645 (±19)	642 (±20)	642 (±20)
low-Al	An ₃₅	647 (±30)	654 (±19)	651 (±21)	651 (±20)
low-Al	An ₄₀	659 (±30)	667 (±20)	664 (±21)	664 (±21)
low-Al	An ₄₅	673 (±31)	681 (±21)	678 (±22)	678 (±21)
high-Al	An ₃₀	732 (±20)	724 (±13)	719 (±14)	711 (±15)
high-Al	An ₃₅	743 (±21)	735 (±14)	729 (±14)	721 (±15)
high-Al	An ₄₀	758 (±21)	750 (±14)	744 (±14)	736 (±16)
high-Al	An ₄₅	776 (±22)	767 (±15)	760 (±15)	752 (±16)
<i>Olsen et al. (1984)</i>					
low-Al		652 (±30)	679 (±28)	669 (±22)	669 (±17)
high-Al		743 (±16)	763 (±13)	758 (±20)	753 (±30)

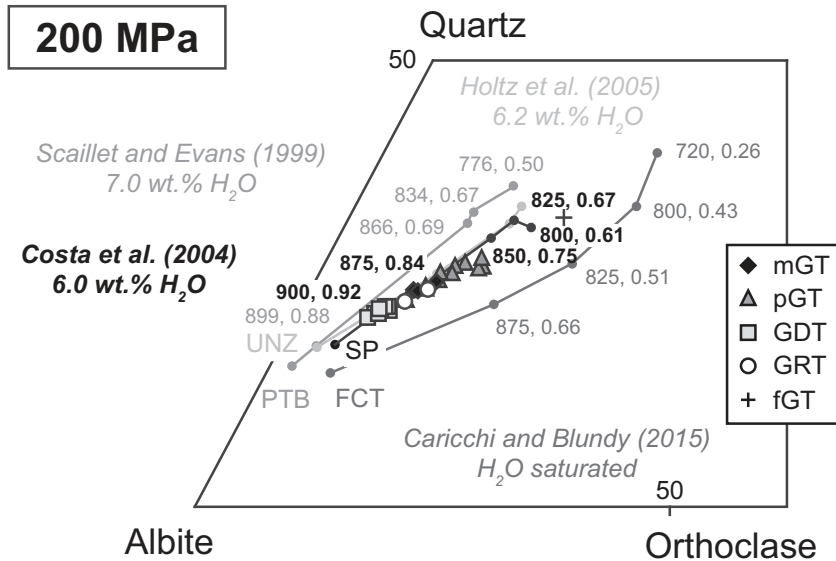


Fig. 16. Compositions of TK bulk-rock and liquids from experimental studies projected into the ternary Qtz–Ab–Or system. The ternary projection is corrected for anorthite following [Blundy & Cashman \(2001\)](#). The TK samples are consistent with the liquids of [Costa et al. \(2004\)](#) and [Holtz et al. \(2005\)](#). Temperatures are listed in degrees Celsius followed by the melt fraction after the comma. TK samples plot between 850 and 900°C. UNZ, Unzen; PTB, Pinatubo; SP, Volcán San Pedro; FCT, Fish Canyon Tuff.

estimates obtained from the semi-empirical Ti-in-hornblende thermometer of Otten (1984; Table 7), with the exception of amphiboles from mGT. The HB94-A and HB94-B thermometers produce temperature estimates that correlate with or are higher than the semi-empirical

temperature calibrations (Otten, 1984). This is not the case for the mGT unit, which appears to have crystallized under slightly different magmatic conditions. HB94-B produces a distribution of temperature estimates that is close to unimodal for the analysed sample

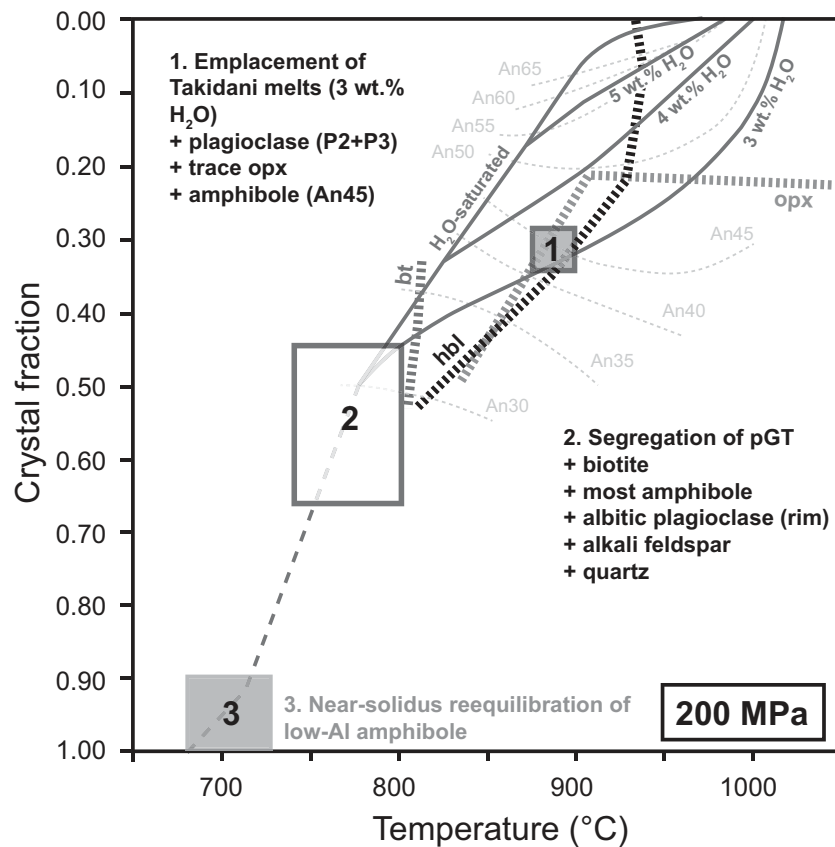


Fig. 17. Magmatic evolution of TK plotted in a binary diagram of crystal fraction vs temperature. Crystal fraction, temperature, An contents and phase stability fields are derived from the experiments of [Costa et al. \(2004\)](#). The melt evolution is projected for bulk-rock water contents of 3, 4, 5 and 6 wt %. Liquidus temperatures are calculated using Rhyolite-MELTS ([Gualda et al., 2012](#); [Ghiorso & Gualda, 2015](#)). Water saturation of rhyolitic melts is calculated to be about 6 wt % using VolatileCalc.

(Fig. 15) and shows peaks between 750 and 810°C for anorthite 30 and 45 mol %, respectively.

Experimental studies

Chemical analyses of the TK were compared with several relevant experimental and petrological studies ([Whitney, 1975, 1988](#); [Sisson & Grove, 1993](#); [Scaillet & Evans, 1999](#); [Costa et al., 2004](#); [Holtz et al., 2005](#); [Caricchi & Blundy, 2015](#)) to assess further the P – T – H_2O conditions at and after emplacement. We projected the residual melts from various experimental studies, equilibrated at different temperatures at around 200 MPa, in the haplogranitic system together with the whole-rock compositions of the TK rocks by calculating their normative Qtz–Ab–Or abundances (i.e. CIPW; Fig. 16). All calculations are corrected for the effect of anorthite in the Qtz–Ab–Or ternary projection ([Blundy & Cashman, 2001](#)). Good correlations of the TK samples are observed with experimental liquids (at or near water saturation) synthesized at 200 MPa using compositions from Unzen Volcano ([Holtz et al., 2005](#)) and Volcán San Pedro ([Costa et al., 2004](#)). The TK samples exhibit compositional variability within this ternary system compatible with crystallization within a temperature range of between 850 and 900°C, higher than the temperatures obtained by hornblende thermometry (Fig. 15). The TK

plagioclase grains span a range of compositions very similar to those obtained experimentally by [Costa et al. \(2004\)](#). However, in the experiments hornblende contains more than 8 wt % of Al_2O_3 and is the liquidus phase for water content above 4 wt % (Fig. 17; [Costa et al., 2004](#)). The mineral chemistry of hornblende from the experiments differs significantly from the high-Al amphiboles in the TK. This, together with microscopic observations, suggests that the TK amphiboles crystallized after plagioclase and potentially orthopyroxene (Fig. 11c). This implies that at emplacement the magma was not water-saturated and must have contained less than 4 wt % water ([Newman & Lowenstern, 2002](#)). During cooling and crystallization, the water content progressively increased until amphibole (>4 wt %) and biotite saturation (>5.5 wt %) was reached (Fig. 17).

P – T – H_2O summary

Our detailed comparison of bulk-rock and mineral chemistry, available thermometers, barometers and experimental data allows us to infer the pressure of emplacement and the evolution of temperature and water content of the residual melt within the TK. The calculated crystallization conditions suggest that different pulses of chemically distinct magmas (at least two main pulses) were emplaced at about 200 MPa and

temperatures between 850 and 900°C with bulk water contents of approximately 3–4 wt % (Fig. 17; Costa *et al.*, 2004). Plagioclase stabilized first (i.e. phenocrysts $>An_{50}$) followed by orthopyroxene. Amphiboles with Al_2O_3 contents above 8 wt % started crystallizing at An contents of about 45 mol % and temperature of about 850°C (Fig. 17). The sharp drop in An content observed in plagioclase rims to about 30 mol % indicates that the magma cooled fairly rapidly to temperatures below 800°C, at which point the water content of the residual melt was appropriate to crystallize biotite (>5.5 wt %). Microscopic observations and temperature calculations (with An_{40}) also show that most amphiboles record crystallization temperatures below 800°C (Fig. 15), suggesting that the TK magmas spent significantly more time below 800°C to crystallize amphibole than above 800°C. Considering the relatively small amount of crystallization occurring between 900 and 800°C for a water-undersaturated magma with about 3 wt % H_2O (or in equilibrium with a mixed H_2O – CO_2 fluid and a water activity of about 0.5; Riker *et al.*, 2015), we can expect a relatively rapid temperature drop within this range owing to the limited thermal buffering provided by the latent heat of crystallization (Huber *et al.*, 2009; Caricchi & Blundy, 2015). In contrast, the rate of latent heat release produced by crystallization increases below 800°C, prolonging the residence time of magma within this temperature range (Lee *et al.*, 2015) and leading to the distribution of amphibole compositions (Fig. 15). Moreover, at temperatures below 800°C magma crystallinities would have reached values in excess of 50 wt % (Fig. 17; Costa *et al.*, 2004). At such high crystallinity the rheological locking of the system would account for the homogeneous composition of the plagioclase rims observed in the TK (Figs 8 and 9).

From emplacement to eruption

Emplacement and growth of the intrusion

Many studies of sill emplacement and pluton growth have illustrated that large magma reservoirs are most probably constructed incrementally over ten thousand to millions of years (Bachl *et al.*, 2001; Coleman *et al.*, 2004; Glazner *et al.*, 2004; de Saint-Blanquat *et al.*, 2006; Kavanagh *et al.*, 2006; Matzel *et al.*, 2006; Lipman, 2007; Pasquare & Tibaldi, 2007; Menand, 2008, 2011; Michel *et al.*, 2008; Annen, 2009, 2011; Leuthold *et al.*, 2012; Annen *et al.*, 2015; Menand *et al.*, 2015). The TK is petrochemically stratified, suggesting an incremental growth of the magma reservoir. The mGT unit has the highest $^{87}Sr/^{86}Sr$ within the TK; it is isotopically distinct from other units and has a peculiar mineral chemistry. Moreover, barometric calculations suggest that this unit was emplaced under the deepest conditions. Reverse zoned plagioclases in mGT indicate that the magma was reheated after emplacement and, therefore, we suggest that the mGT was the first unit emplaced at the roof of the intrusion. During subsequent magma injection, possibly at shallower depths, a certain amount of

mingling must have occurred between the mGT magma and the under-accreted units (i.e. pGT and GDT). For instance, whereas no or only very few of the P2 plagioclase grains—characteristic of GDT and pGT units—are present within the mGT unit, some P1 phenocrysts are found within pGT. This suggests that mGT was still partially molten when the underlying units were emplaced.

Previous researchers have argued that the construction of the TK reservoir must have occurred within ~600 kyr after the deposition of the 2.4 Ma Hotaka Andesite (Harayama *et al.*, 2003) but before the deposition of the genetically related Nyukawa PFD and Chayano–Ebisutoge Pyroclastic Deposits at about 1.76–1.75 Ma (Nagahashi, 1995; Kataoka *et al.*, 2001; Kimura & Nagahashi, 2007). Zircon crystallization ages of the TK ($1.54 \text{ Ma} \pm 0.23 \text{ Ma}$; Sano *et al.*, 2002) suggest that magmatic conditions were maintained after the eruption of these voluminous volcanic units. Older K–Ar ages of amphibole (i.e. 1.9 Ma; Harayama, 1992) may therefore represent older and solidified parts of the TK that had cooled below 580°C (closure temperature of K–Ar in hornblende; Harayama, 1992). This would imply that parts of the pluton had to be re-melted.

We argue that the TK was incrementally under-accreted to form one large coherent magma reservoir. The top mGT unit represents the first magma batch, which was still partially molten upon the intrusion of subsequent units (e.g. GDT and pGT). The granitic units at the base of the pluton may present a third and last period of magma injection.

Origin of pGT: evidence for internal differentiation and segregation of upper crustal residual melt

A unique feature of the pGT unit is the presence of features suggesting a two-stage cooling from an initially crystal-free or crystal-poor magma. All other magma bodies of the TK body show evidence for steady cooling from, presumably, crystal-rich magma upon intrusion. These differences suggest that a detailed study of the pGT may reveal important information about transport of melt in the TK pluton. As discussed below, a combination of field relations, mineral chemistry and mass-balance calculations provides strong evidence to suggest that pGT formed as a consequence of internal differentiation followed by segregation and accumulation of the interstitial melt as a discrete magma body. If correct, the GDT–pGT units present a rare example of upper crustal melt segregation from a stagnant crystal-liquid mush, which in turn lends credence to the multiple theoretical and numerical studies that have suggested such a process (Hildreth, 1981; Marsh, 1981; Brophy, 1991; Srogi & Lutz, 1996; Vigneresse *et al.*, 1996; Bachmann & Bergantz, 2004, 2008; Hildreth & Wilson, 2007; Dufek & Bachmann, 2010; Deering *et al.*, 2011; Gelman *et al.*, 2014; Lee & Morton, 2015).

Three lines of evidence support an origin of the pGT through internal differentiation of the GDT, followed by melt extraction. First, and most significant, is the

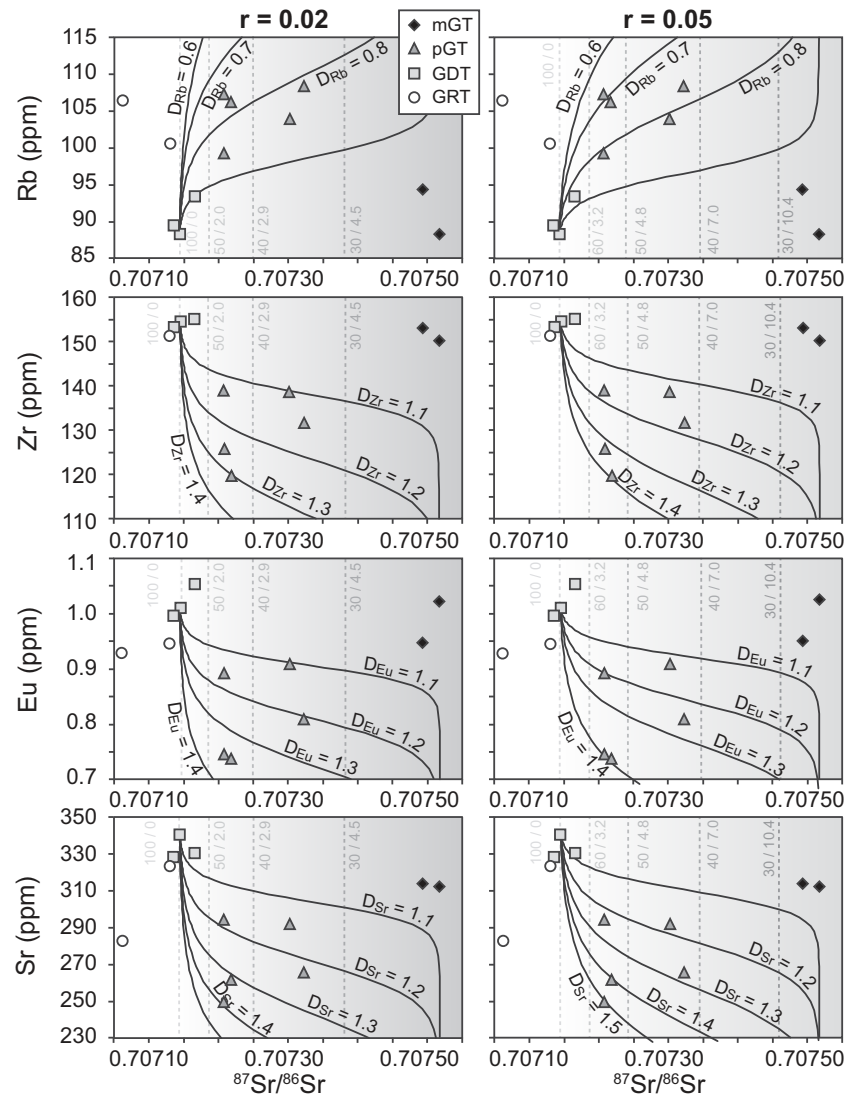


Fig. 18. Assimilation and fractional crystallization (AFC) modeling of TK melts after DePaolo (1981). Trace element and isotopic trends of pGT are reproduced with 45–65% of crystal fractionation of GDT and 2–6% of assimilation of mGT.

sigmoidal variation in both major and trace elements defined by the GRT, GDT, pGT and mGT shown in Fig. 5. This is entirely consistent with the successive intrusion of three different bodies of granodioritic magma, which underwent *in situ* crystallization. For whatever reason, the first and third intrusions underwent complete crystallization to form the mGT and GRT whereas the second intrusion underwent incomplete crystallization, followed by melt extraction and segregation. The pGT unit represents the more evolved extracted melt whereas the GDT represents the seemingly less evolved cumulate remainder, which together lead to the sigmoidal pattern. Second, the gradual contact between the GDT and pGT is consistent with extraction and segregation of an interstitial melt. Third, the fact that the plagioclase rims of the GDT are compositionally identical to the fine-grained matrix plagioclase of the pGT strongly suggests a genetic relation between the two.

Radiogenic isotope compositions and assimilation–fractional crystallization (AFC) models (DePaolo, 1981)

support fractionation-dominated differentiation (Fig. 18). The isotopic and trace element variation of the GDT, pGT and mGT can be explained by 45–65% fractional crystallization of GDT magma, accompanied by a small amount (2–6%) of incorporation of the overlying mGT. Given that P1 is the only plagioclase type in mGT, its presence in pGT is consistent with the assimilation of partially molten mGT required by the AFC calculations (Fig. 18). The higher silica content and lower Zr concentration of the pGT (Fig. 5), with respect to the GDT, suggest that the residual melt was extracted from the crystallizing granodioritic magma at a temperature near or lower than its zircon saturation temperature ($731^{\circ}\text{C} \pm 7^{\circ}\text{C}$; Watson & Harrison, 1983). This temperature is a lower limit because the calculations of zircon saturation were performed considering the bulk-rock composition (Harrison *et al.*, 2007).

Based upon a comparison with the experimental results of Costa *et al.* (2004), we can attempt to identify the conditions at which the extraction of the residual melt

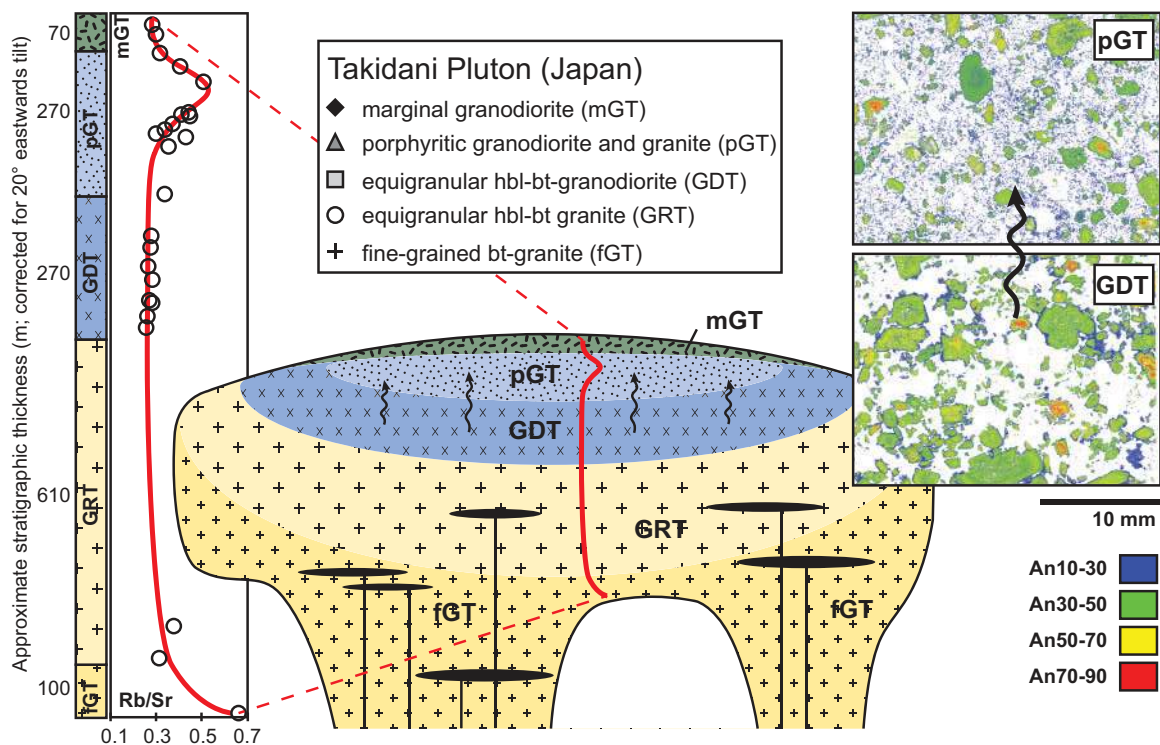


Fig. 19. Cross-section of the TK including melt segregation evidence from the lower granodiorite (GDT) to the overlying porphyritic unit (pGT) illustrated through sigmoidal variations in whole-rock chemistry. GDT and pGT contain the same population of plagioclase phenocrysts (i.e. P2). Overgrowth rims of plagioclase in GDT have the same composition as matrix plagioclase in pGT, further supporting upwards migration of interstitial melt. This figure is based on the schematic illustration of a crystal mush from Hildreth & Wilson (2007).

occurred. Partly resorbed bytownite cores in plagioclase (up to An_{90}) can be reconciled with the ascent of water-undersaturated magma containing a few plagioclase crystals formed at relatively high pressure (Sisson & Grove, 1993; Nandedkar *et al.*, 2014). These anorthite-rich cores (<1 total area %; Table 5) change rapidly into andesine compositions (An_{50-40}) within the plagioclase domain characterized by oscillatory growth zones. In addition, the anorthite content of plagioclase included in amphibole is never higher than 45 mol %, suggesting that amphibole becomes stable when An_{45} plagioclase crystallized. According to Costa *et al.* (2004) contemporaneous crystallization of amphibole and An_{45} occurs at about 850°C for an H_2O content of 4 wt % (Fig. 17). Traces of orthopyroxene were found within amphibole phenocrysts. Orthopyroxene is stable at higher temperature than amphibole: at water contents of about 3 wt % its presence indicates temperatures above 925°C. Altogether these lines of evidence suggest that after a period of crystallization at relatively high pressure (700 MPa; Nandedkar *et al.*, 2014), water-undersaturated melt was transported to shallower depths where the crystallization of An_{45} plagioclase occurred contemporaneously with amphibole at ~850°C (Figs 15 and 17).

Following the temperature–crystallinity diagram obtained from the experiments of Costa *et al.* (2004), the TK magmas would have reached water saturation at about 800°C and 50 wt % crystals, after progressive cooling and the onset of amphibole crystallization

(Fig. 17). The chemical variations between the GDT and pGT can be explained by crystal fractionation of up to 65 wt % (Fig. 18).

These lines of evidence suggest that the extraction of the residual melt from the GDT occurred at crystallinities between 45 and 65 wt % and resulted in the formation of the pGT (Figs 18 and 19), which is in agreement with the optimal extraction window identified by the thermomechanical models of Dufek & Bachmann (2010). The coincidence between the crystallinity at which melt extraction seem to have occurred and the achievement of water saturation suggests that the residual melt extraction may have been triggered by the exsolution of excess volatiles (Sisson & Bacon, 1999; Fowler *et al.*, 2015).

Pressure quenching and the porphyritic texture of pGT

One of the most striking textural observations of the various units of the TK is the gradual transition from a holocrystalline to a porphyritic texture seen from the top of GDT into pGT. The fine-grained matrix of the porphyritic unit is difficult to explain by temperature quenching given the gradual transition of the major and trace element geochemistry observed from GDT to pGT (Fig. 5). An alternative explanation for the fine-grained nature of pGT is a sudden decompression that would result in the rapid exsolution of H_2O (Newman &

Lowenstern, 2002), an increase of liquidus temperature and consequent rapid crystallization. Because the transition from holocrystalline to porphyritic is gradual, such decompression cannot be associated with the rise of magma toward the surface. A viable process producing a rapid pressure drop and triggering rapid crystallization could be an eruption. The observation that the proportion of phenocrysts in the pGT varies across the unit suggests that the melt was mobile before it was quenched.

CONCLUSIONS AND FUTURE WORK

Our detailed field and petrographic investigations, bulk-rock and mineral analyses of the TK along the Shiradashi-zawa valley lead to the following conclusions regarding its magmatic evolution.

1. The TK represents an evolved magma reservoir in the upper crust comprising five distinct units of granodioritic to granitic composition. The pluton was emplaced incrementally at about 9.5–6.5 km depth. The intrusion of successive magma pulses led to the formation of one large, interconnected magma body.
2. The chemical variations observed in the upper part of the TK are best explained in terms of fractional crystallization acting together with segregation of the residual melt. The chemical and isotopic compositions of the pGT are best explained by its extraction during crystallization of the GDT (45–65 wt % crystals) after minor assimilation of 2–6 wt % of the overlying mGT unit (Fig. 19).
3. Rapid crystallization must have occurred to create the fine-grained porphyritic texture of the pGT near the roof of the TK. A volcanic eruption is a plausible mechanism that can lower the pressure, trigger volatile exsolution and cause rapid crystallization of the remaining melt in the magma reservoir.

Our results suggest that chemical evolution towards the roof of the TK was controlled by melt extraction from crystallizing magma in the upper crust. The presence of a porphyritic unit might be evidence for volcanic activity, making the TK an exciting location to investigate the magmatic build-up to caldera-forming eruptions. A study of trace element variations (i.e. Sr and Eu) in single zoned feldspar grains is currently being undertaken with the aim of shedding more light on the Takidani magmatic system and its genetic association with the Nyukawa and Chayano–Ebisutoge deposits (Kimura & Nagahashi, 2007).

ACKNOWLEDGEMENTS

Many thanks go to James Brophy, Cin-Ty Lee and Jean-Louis Vigneresse for their constructive feedback that significantly clarified this paper. We would also like to acknowledge Jean-Marie Boccard and Fabio-Marco

Capponi at the University of Geneva for their assistance with sample preparation and XRF analyses, and Alexey Ulianov at the University of Lausanne for his assistance with LA-ICP-MS analyses.

FUNDING

This study was supported by the SNSF grant 200021_150204. L.C. acknowledges additional funding from the European Research Council (ERC) under the European Union's Horizon 2020 research and innovation program (grant agreement No. 677493, FEVER).

SUPPLEMENTARY DATA

Supplementary data for this paper are available at *Journal of Petrology* online.

REFERENCES

- Anderson, J. L. (1996). Status of thermobarometry in granitic batholiths. *Geological Society of America Special Papers* **315**, 125–138.
- Anderson, J. L. & Smith, D. R. (1995). The effects of temperature and fO_2 on the Al-in-hornblende barometer. *American Mineralogist* **80**, 549–559.
- Anderson, J. L., Barth, A. P., Wooden, J. L. & Mazdab, F. (2008). Thermometers and thermobarometers in granitic systems. In: Putirka, K. D. & Tepley, F. J., III (eds) *Minerals, Inclusions and Volcanic Processes. Mineralogical Society of America and Geochemical Society, Reviews in Mineralogy and Geochemistry* **69**, 121–142.
- Annen, C. (2009). From plutons to magma chambers: Thermal constraints on the accumulation of eruptible silicic magma in the upper crust. *Earth and Planetary Science Letters* **284**, 409–416.
- Annen, C. (2011). Implications of incremental emplacement of magma bodies for magma differentiation, thermal aureole dimensions and plutonism–volcanism relationships. *Tectonophysics* **500**, 3–10.
- Annen, C., Blundy, J. D., Leuthold, J. & Sparks, R. S. J. (2015). Construction and evolution of igneous bodies: Towards an integrated perspective of crustal magmatism. *Lithos* **230**, 206–221.
- Arce, J. L., Gardner, J. E. & Macías, J. L. (2013). Pre-eruptive conditions of dacitic magma erupted during the 21.7 ka Plinian event at Nevado de Toluca volcano, Central Mexico. *Journal of Volcanology and Geothermal Research* **249**, 49–65.
- Bachl, C. A., Miller, C. F., Miller, J. S. & Faulds, J. E. (2001). Construction of a pluton: Evidence from an exposed cross section of the Searchlight pluton, Eldorado Mountains, Nevada. *Geological Society of America Bulletin* **113**, 1213–1228.
- Bachmann, O. & Bergantz, G. (2004). On the origin of crystal-poor rhyolites: extracted from batholithic crystal mushes. *Journal of Petrology* **45**, 1565–1582.
- Bachmann, O. & Bergantz, G. W. (2008). Rhyolites and their source mushes across tectonic settings. *Journal of Petrology* **49**, 2277–2285.
- Bachmann, O. & Dungan, M. A. (2002). Temperature-induced Al-zoning in hornblendes of the Fish Canyon magma, Colorado. *American Mineralogist* **87**, 1062–1076.
- Baker, J., Peate, D., Waight, T. & Meyzen, C. (2004). Pb isotopic analysis of standards and samples using a ^{207}Pb – ^{204}Pb

- double spike and thallium to correct for mass bias with a double-focusing MC-ICP-MS. *Chemical Geology* **211**, 275–303.
- Bando, M. & Tsuchiya, N. (2000). Petrologic characterization of the Quaternary volcanic–plutonic system: The Takidani Pluton and associated volcanic rocks in the Japan Alps, Japan. *Proceedings World Geothermal Congress 2000. Kyushu–Tohoku, Japan*, 3637–3641.
- Bando, M., Bignall, G., Sekine, K. & Tsuchiya, N. (2003). Petrography and uplift history of the Quaternary Takidani Granodiorite: could it have hosted a supercritical (HDR) geothermal reservoir? *Journal of Volcanology and Geothermal Research* **120**, 215–234.
- Barboni, M. & Schoene, B. (2014). Short eruption window revealed by absolute crystal growth rates in a granitic magma. *Nature Geoscience* **7**, 524–528.
- Bernet, M. & Garver, J. I. (2005). Fission-track analysis of detrital zircon. In: Reiners, P. W. & Ehlers, T. A. (eds) *Low-temperature Thermochronology: Techniques, Interpretations and Applications*. Mineralogical Society of America and Geochemical Society, *Reviews in Mineralogy and Geochemistry* **58**, 205–237.
- Blundy, J. D. & Cashman, K. (2001). Ascent-driven crystallisation of dacite magmas at Mount St Helens, 1980–1986. *Contributions to Mineralogy and Petrology* **140**, 631–650.
- Blundy, J. D. & Holland, T. J. B. (1990). Calcic amphibole equilibria and a new amphibole–plagioclase geothermometer. *Contributions to Mineralogy and Petrology* **104**, 208–224.
- Brophy, J. G. (1991). Composition gaps, critical crystallinity, and fractional crystallization in orogenic (calc-alkaline) magmatic systems. *Contributions to Mineralogy and Petrology* **109**, 173–182.
- Caricchi, L. & Blundy, J. (2015). The temporal evolution of chemical and physical properties of magmatic systems. In: Caricchi, L. & Blundy, J. D. (eds) *Chemical, Physical and Temporal Evolution of Magmatic Systems*. Geological Society, London, *Special Publications* **422**, 1–15.
- Cashman, K. V. & Giordano, G. (2014). Calderas and magma reservoirs. *Journal of Volcanology and Geothermal Research* **288**, 28–45.
- Chiaradia, M., Müntener, O. & Beate, B. (2011). Enriched basaltic andesites from mid-crustal fractional crystallization, recharge, and assimilation (Pilavo volcano, Western Cordillera of Ecuador). *Journal of Petrology* **52**, 1107–1141.
- Christopher, T. E., Blundy, J., Cashman, K., Cole, P., Edmonds, M., Smith, P. J., Sparks, R. S. J. & Stinton, A. (2015). Crustal-scale degassing due to magma system destabilization and magma–gas decoupling at Soufrière Hills Volcano, Montserrat. *Geochemistry, Geophysics, Geosystems* **16**, 1–15.
- Coleman, D. S., Gray, W. & Glazner, A. F. (2004). Rethinking the emplacement and evolution of zoned plutons: Geochronologic evidence for incremental assembly of the Tuolumne Intrusive Suite, California. *Geology* **32**, 433–436.
- Coleman, D. S., Bartley, J. M., Glazner, A. F. & Pardue, M. J. (2012). Is chemical zonation in plutonic rocks driven by changes in source magma composition or shallow-crustal differentiation? *Geosphere* **8**, 1568–1587.
- Costa, F., Scaillet, B. & Pichavant, M. (2004). Petrological and experimental constraints on the pre-eruption conditions of Holocene dacite from Volcan San Pedro (36°S, Chilean Andes) and the importance of sulphur in silicic subduction-related magmas. *Journal of Petrology* **45**, 855–881.
- Deering, C. D., Bachmann, O., Dufek, J. & Gravley, D. M. (2011). Rift-related transition from andesite to rhyolite volcanism in the Taupo Volcanic Zone (New Zealand) controlled by crystal–melt dynamics in mush zones with variable mineral assemblages. *Journal of Petrology* **52**, 2243–2263.
- DePaolo, D. J. (1981). Trace element and isotopic effects of combined wallrock assimilation and fractional crystallization. *Earth and Planetary Science Letters* **53**, 189–202.
- de Saint-Blanquat, M., Habert, G., Horsman, E., Morgan, S. S., Tikoff, B., Launeau, P. & Gleizes, G. (2006). Mechanisms and duration of non-tectonically assisted magma emplacement in the upper crust: The Black Mesa pluton, Henry Mountains, Utah. *Tectonophysics* **428**, 1–31.
- Dufek, J. & Bachmann, O. (2010). Quantum magmatism: Magmatic compositional gaps generated by melt–crystal dynamics. *Geology* **38**, 687–690.
- Ellis, B. S., Bachmann, O. & Wolff, J. A. (2014). Cumulate fragments in silicic ignimbrites: The case of the Snake River Plain. *Geology* **42**, 431–434.
- Fowler, A. C., Rust, A. C. & Vynnycky, M. (2015). The formation of vesicular cylinders in pahoehoe lava flows. *Geophysical and Astrophysical Fluid Dynamics* **109**, 39–61.
- Gelman, S. E., Deering, C. D., Bachmann, O., Huber, C. & Gutiérrez, F. J. (2014). Identifying the crystal graveyards remaining after large silicic eruptions. *Earth and Planetary Science Letters* **403**, 299–306.
- Ghiorso, M. S. & Gualda, G. A. R. (2015). An H₂O–CO₂ mixed fluid saturation model compatible with rhyolite-MELTS. *Contributions to Mineralogy and Petrology* **169**, 53.
- Glazner, A. F., Bartley, J. M., Coleman, D. S., Gray, W. & Taylor, R. Z. (2004). Are plutons assembled over millions of years by amalgamation from small magma chambers? *GSA Today* **14**, 1–8.
- Gualda, G. A. R., Ghiorso, M. S., Lemons, R. V. & Carley, T. L. (2012). Rhyolite-MELTS: a modified calibration of MELTS optimized for silica-rich, fluid-bearing magmatic systems. *Journal of Petrology* **53**, 875–890.
- Hammarstrom, J. M. & Zen, E. (1986). Aluminum in hornblende: An empirical igneous geobarometer. *American Mineralogist* **71**, 1297–1313.
- Harayama, S. (1990). *Geology of the Kamigochi district with geological sheet map at 1:50000*. Geological Survey of Japan, 175 p.
- Harayama, S. (1992). Youngest exposed granitoid pluton on Earth: Cooling and rapid uplift of the Pliocene–Quaternary Takidani Granodiorite in the Japan Alps, central Japan. *Geology* **20**, 657–660.
- Harayama, S. (1994). Cooling history of the youngest exposed pluton in the world—the Plio-Pleistocene Takidani Granodiorite (Japan Alps, central Japan). *Memoirs of the Geological Society of Japan* **43**, 87–97.
- Harayama, S., Takeuchi, M., Nakano, S., Sato, T. & Takizawa, F. (1991). *Geology of the Yurigatake district with geological sheet map at 1:50000*. Geological Survey of Japan, 190 p.
- Harayama, S., Wada, H. & Yamaguchi, Y. (2003). Trip A1: Quaternary and Pliocene granites in the Northern Japan Alps. *Hutton Symposium V, Field Guidebook*. Geological Survey of Japan, Interim-Report no. 28, 3–21.
- Harrison, T. M., Watson, E. B. & Aikman, A. B. (2007). Temperature spectra of zircon crystallization in plutonic rocks. *Geology* **35**, 635–638.
- Hildreth, W. (1981). Gradients in silicic magma chambers: Implications for lithospheric magmatism. *Journal of Geophysical Research: Solid Earth* **86**, 10153–10192.
- Hildreth, W. (2004). Volcanological perspectives on Long Valley, Mammoth Mountain, and Mono Craters: several contiguous but discrete systems. *Journal of Volcanology and Geothermal Research* **136**, 169–198.
- Hildreth, W. & Wilson, C. J. N. (2007). Compositional zoning of the Bishop Tuff. *Journal of Petrology* **48**, 951–999.

- Holland, T. & Blundy, J. D. (1994). Non-ideal interactions in calcic amphiboles and their bearing on amphibole–plagioclase thermometry. *Contributions to Mineralogy and Petrology* **116**, 433–447.
- Holtz, F., Sato, H., Lewis, J., Behrens, H. & Nakada, S. (2005). Experimental petrology of the 1991–1995 Unzen dacite, Japan. Part I: Phase relations, phase composition and pre-eruptive conditions. *Journal of Petrology* **46**, 319–337.
- Huber, C., Bachmann, O. & Manga, M. (2009). Homogenization processes in silicic magma chambers by stirring and mushification (latent heat buffering). *Earth and Planetary Science Letters* **283**, 38–47.
- Jackson, S. E. (2008a). Calibration strategies for elemental analysis by LA-ICP-MS. In: Sylvester, P. J. (ed.) *Laser Ablation-ICP-Mass Spectrometry in the Earth Sciences: Current Practices and Outstanding Issues*. Mineralogical Association of Canada Short Course Series **40**, 169–188.
- Jackson, S. E. (2008b). LAMTRACE data reduction software for LA-ICP-MS. In: Sylvester, P. J. (ed.) *Laser Ablation-ICP-Mass Spectrometry in the Earth Sciences: Current Practices and Outstanding Issues*. Mineralogical Association of Canada Short Course Series **40**, 305–307.
- Jackson, S. E., Longerich, H. P., Dunning, G. R. & Fryer, B. J. (1992). The application of laser-ablation microprobe-inductively coupled plasma-mass spectrometry (LAM-ICP-MS) to *in situ* trace element determination in minerals. *Canadian Mineralogist* **30**, 1049–1064.
- Johnson, M. C. & Rutherford, M. J. (1989). Experimentally determined conditions in the Fish Canyon Tuff, Colorado, magma chamber. *Journal of Petrology* **30**, 711–737.
- Kano, S., Kishi, K., Saito, K., Shiro, C., Tsuchiya, N. & Nakatsuka, K. (2000). Field observation of a cooling joint system in the Quaternary Takidani Pluton, Japan. *Proceedings World Geothermal Congress 2000. Kyushu-Tohoku, Japan*, pp. 3761–3766.
- Kataoka, K., Nagahashi, Y. & Yoshikawa, S. (2001). An extremely large magnitude eruption close to the Plio-Pleistocene boundary: reconstruction of eruptive style and history of the Ebisutoge–Fukuda tephra, central Japan. *Journal of Volcanology and Geothermal Research* **107**, 47–69.
- Kavanagh, J. L., Menand, T. & Sparks, R. S. J. (2006). An experimental investigation of sill formation and propagation in layered elastic media. *Earth and Planetary Science Letters* **245**, 799–813.
- Kawakatsu, K. & Yamaguchi, Y. (1987). Successive zoning of amphiboles during progressive oxidation in the Daito–Yokota granitic complex, San-in belt, southwest Japan. *Geochimica et Cosmochimica Acta* **51**, 535–540.
- Kimura, J.-I. & Nagahashi, Y. (2007). Origin of a voluminous iron-enriched high-K rhyolite magma erupted in the North Japan Alps at 1.75 Ma: Evidence for upper crustal melting. *Journal of Volcanology and Geothermal Research* **167**, 81–99.
- Leake, B. E., Woolley, A. R. & Arps, C. E. S. et al. (1997). Nomenclature of Amphiboles: Report of the Subcommittee on Amphiboles of the International Mineralogical Association Commission on New Minerals and Mineral Names. *Canadian Mineralogist* **35**, 219–246.
- Lee, C.-T. A. & Morton, D. M. (2015). High silica granites: Terminal porosity and crystal settling in shallow magma chambers. *Earth and Planetary Science Letters* **409**, 23–31.
- Lee, C.-T. A., Morton, D. M., Farnier, M. J. & Moitra, P. (2015). Field and model constraints on silicic melt segregation by compaction/hindered settling: The role of water and its effect on latent heat release. *American Mineralogist* **100**, 1762–1777.
- Le Maitre, R. W. (1989). *A Classification of Igneous Rocks and Glossary of Terms: Recommendations of the International Union of Geological Sciences Subcommission on the Systematics of Igneous Rocks*. Blackwell, 193 p.
- Leuthold, J., Müntener, O., Baumgartner, L. P., Putlitz, B., Ovtcharova, M. & Schaltegger, U. (2012). Time resolved construction of a bimodal laccolith (Torres del Paine, Patagonia). *Earth and Planetary Science Letters* **325–326**, 85–92.
- Lipman, P. W. (2007). Incremental assembly and prolonged consolidation of Cordilleran magma chambers: Evidence from the Southern Rocky Mountain volcanic field. *Geosphere* **3**, 42–70.
- Longerich, H. P., Gunther, D. & Jackson, S. E. (1996). Elemental fractionation in laser ablation inductively coupled plasma mass spectrometry. *Fresenius' Journal of Analytical Chemistry* **355**, 538–542.
- Marsh, B. D. (1981). On the crystallinity, probability of occurrence, and rheology of lava and magma. *Contributions to Mineralogy and Petrology* **78**, 85–98.
- Martin, R. F. (2007). Amphiboles in the igneous environment. In: Hawthorne, F. C., Oberti, R., Della Ventura, G. & Mottana, A. (eds) *Amphiboles: Crystal Chemistry, Occurrence and Health Issues*. Mineralogical Society of America and Geochemical Society, *Reviews in Mineralogy and Geochemistry* **67**, 323–358.
- Matzel, J. E. P. P., Bowring, S. A. & Miller, R. B. (2006). Time scales of pluton construction at differing crustal levels: Examples from the Mount Stuart and Tenpeak intrusions, North Cascades, Washington. *Geological Society of America Bulletin* **118**, 1412–1430.
- Melekhova, E., Annen, C. & Blundy, J. (2013). Compositional gaps in igneous rock suites controlled by magma system heat and water content. *Nature Geoscience* **6**, 385–390.
- Menand, T. (2008). The mechanics and dynamics of sills in layered elastic rocks and their implications for the growth of laccoliths and other igneous complexes. *Earth and Planetary Science Letters* **267**, 93–99.
- Menand, T. (2011). Physical controls and depth of emplacement of igneous bodies: A review. *Tectonophysics* **500**, 11–19.
- Menand, T., Annen, C. & de Saint Blanquat, M. (2015). Rates of magma transfer in the crust: Insights into magma reservoir recharge and pluton growth. *Geology* **43**, 199–203.
- Michel, J., Baumgartner, L., Putlitz, B., Schaltegger, U. & Ovtcharova, M. (2008). Incremental growth of the Patagonian Torres del Paine laccolith over 90 k.y. *Geology* **36**, 459–462.
- Nagahashi, Y. (1995). Plio-Pleistocene volcanoclastic formation in the Takayama Basin, Gifu prefecture—stratigraphy and petrography. *Earth Science (Chikyu Kagaku)* **2**, 109–124.
- Nagahashi, Y., Kosaka, T. & Hibi, N. (1996). Correlation of the late Pliocene large-scale pyroclastic flow deposits, Gifu and Nagano prefectures, central Japan—case study of the Nyukawa Pyroclastic Flow Deposit, Ebisutoge Pyroclastic Deposits and their correlative deposits. *Earth Science (Chikyu Kagaku)* **50**, 29–42.
- Nagahashi, Y., Satoguchi, Y. & Yoshikawa, S. (2000). Correlation and stratigraphic eruption age of the pyroclastic flow deposits and widespread volcanic ashes intercalated in the Pliocene–Pleistocene strata, central Japan. *Journal of the Geological Society of Japan* **106**, 51–69.
- Nandedkar, R. H., Ulmer, P. & Müntener, O. (2014). Fractional crystallization of primitive, hydrous arc magmas: an experimental study at 0.7 GPa. *Contributions to Mineralogy and Petrology* **167**, 1015.

- Newman, S. & Lowenstern, J. B. (2002). VolatileCalc: a silicate melt–H₂O–CO₂ solution model written in Visual Basic for Excel. *Computers and Geosciences* **28**, 597–604.
- Otten, M. T. (1984). The origin of brown hornblende in the Artfjället gabbro and dolerites. *Contributions to Mineralogy and Petrology* **86**, 189–199.
- Papale, P. & Barbato, D. (2006). The compositional dependence of the saturation surface of H₂O + CO₂ fluids in silicate melts. *Chemical Geology* **229**, 78–95.
- Pasquaré, F. & Tibaldi, A. (2007). Structure of a sheet–laccolith system revealing the interplay between tectonic and magma stresses at Stardalur Volcano, Iceland. *Journal of Volcanology and Geothermal Research* **161**, 131–150.
- Paterson, S. R., Fowler, T. K., Schmidt, K. L., Yoshinobu, A. S., Yuan, E. S. & Miller, R. B. (1998). Interpreting magmatic fabric patterns in plutons. *Lithos* **44**, 53–82.
- Pirrie, D., Butcher, A. R., Power, M. R., Gottlieb, P. & Miller, G. L. (2004). Rapid quantitative mineral and phase analysis using automated scanning electron microscopy (QemSCAN); potential applications in forensic geoscience. *Geological Society, London, Special Publications* **232**, 123–136.
- Riker, J. M., Blundy, J. D., Rust, A. C., Botcharnikov, R. E. & Humphreys, M. C. S. (2015). Experimental phase equilibria of a Mount St. Helens rhyodacite: a framework for interpreting crystallization paths in degassing silicic magmas. *Contributions to Mineralogy and Petrology* **170**, 6.
- Robinson, P., Schumacher, J. C. & Spear, F. S. (1982). Formulation of electron probe analyses. In: Veblen, D. R. & Ribbe, P. H. (eds) *Amphiboles: Petrology and Experimental Phase Relations*. Mineralogical Society of America, *Reviews in Mineralogy* **9B**, 6–9.
- Sano, Y., Tsutsumi, Y., Terada, K. & Kaneoka, I. (2002). Ion microprobe U–Pb dating of Quaternary zircon: implication for magma cooling and residence time. *Journal of Volcanology and Geothermal Research* **117**, 285–296.
- Scaillet, B. & Evans, B. W. (1999). The 15 June 1991 eruption of Mount Pinatubo. I. Phase equilibria and pre-eruption P–T–fO₂–fH₂O conditions of the dacite magma. *Journal of Petrology* **40**, 381–411.
- Schmidt, M. W. (1992). Amphibole composition in tonalite as a function of pressure: an experimental calibration of the Al-in-hornblende barometer. *Contributions to Mineralogy and Petrology* **110**, 304–310.
- Shane, P. & Smith, V. C. (2013). Using amphibole crystals to reconstruct magma storage temperatures and pressures for the post-caldera collapse volcanism at Okataina volcano. *Lithos* **156–159**, 159–170.
- Sharpe, M. R. (1985). Strontium isotope evidence for preserved density stratification in the main zone of the Bushveld Complex, South Africa. *Nature* **316**, 119–126.
- Sisson, T. W. & Bacon, C. R. (1999). Gas-driven filter pressing in magmas. *Geology* **27**, 613–616.
- Sisson, T. W. & Grove, T. L. (1993). Experimental investigations of the role of H₂O in calc-alkaline differentiation and subduction zone magmatism. *Contributions to Mineralogy and Petrology* **113**, 143–166.
- Solano, J. M. S., Jackson, M. D., Sparks, R. S. J., Blundy, J. D. & Annen, C. (2012). Melt segregation in deep crustal hot zones: A mechanism for chemical differentiation, crustal assimilation and the formation of evolved magmas. *Journal of Petrology* **53**, 1999–2026.
- Spear, F. S. (1981). An experimental study of hornblende stability and compositional variability in amphibolite. *American Journal of Science* **281**, 697–734.
- Spear, F. S. & Kimball, K. L. (1984). RECAMP—a FORTRAN IV program for estimating Fe³⁺ contents in amphiboles. *Computers and Geosciences* **10**, 317–325.
- Srogi, L. & Lutz, T. M. (1996). The role of residual melt migration in producing compositional diversity in a suite of granitic rocks. *Earth and Planetary Science Letters* **144**, 563–576.
- Tanaka, T., Togashi, S., Kamioka, H., et al. (2000). JNdi-1: a neodymium isotopic reference in consistency with LaJolla neodymium. *Chemical Geology* **168**, 279–281.
- Thomas, W. M. & Ernst, W. G. (1990). The aluminium content of hornblende in calc-alkaline granitic rocks: a mineralogical barometer calibrated experimentally to 12 kbars. In: Spencer, R. J. & Chou, I.-M. (eds) *Fluid–Mineral Interactions: A Tribute to H. P. Eugster*. Geochemical Society, *Special Publication* **2**, 59–63.
- Tsuchiya, N. & Fujino, K. (2000). Evaluation of cooling history of the Quaternary Takidani Pluton using thermoluminescence technique. *Proceedings World Geothermal Congress 2000, Kyushu-Tohoku, Japan*, pp. 3939–3944.
- Vigneresse, J. L., Barbey, P. & Cuney, M. (1996). Rheological transitions during partial melting and crystallization with application to felsic magma segregation and transfer. *Journal of Petrology* **37**, 1579–1600.
- Watson, E. B. & Harrison, T. M. (1983). Zircon saturation revisited: temperature and composition effects in a variety of crustal magma types. *Earth and Planetary Science Letters* **64**, 295–304.
- Whitney, J. A. (1975). The effects of pressure, temperature, and XH₂O on phase assemblage in four synthetic rock compositions. *Journal of Geology* **83**, 1–31.
- Whitney, J. A. (1988). The origin of granite: The role and source of water in the evolution of granitic magmas. *Geological Society of America Bulletin* **100**, 1886–1897.
- Wotzlaw, J., Bindeman, I. N., Watts, K. E., Schmitt, A. K., Caricchi, L. & Schaltegger, U. (2014). Linking rapid magma reservoir assembly and eruption trigger mechanisms at evolved Yellowstone-type supervolcanoes. *Geology* **42**, 807–810.
- Yamada, N., Kato, H., Ono, K. & Iwata, O. (1985). K–Ar ages of some Pliocene to Pleistocene felsic volcanic rocks around the Japanese Northern Alps, central Honshu. *Bulletin of the Geological Survey of Japan* **36**, 539–549.
- Zak, J., Paterson, S. R. & Memeti, V. (2007). Four magmatic fabrics in the Tuolumne batholith, central Sierra Nevada, California (USA): Implications for interpreting fabric patterns in plutons and evolution of magma chambers in the upper crust. *Geological Society of America Bulletin* **119**, 184–201.